Naval Research Reviews

Office of Naval Research
Three / 1996
Vol XLVIII

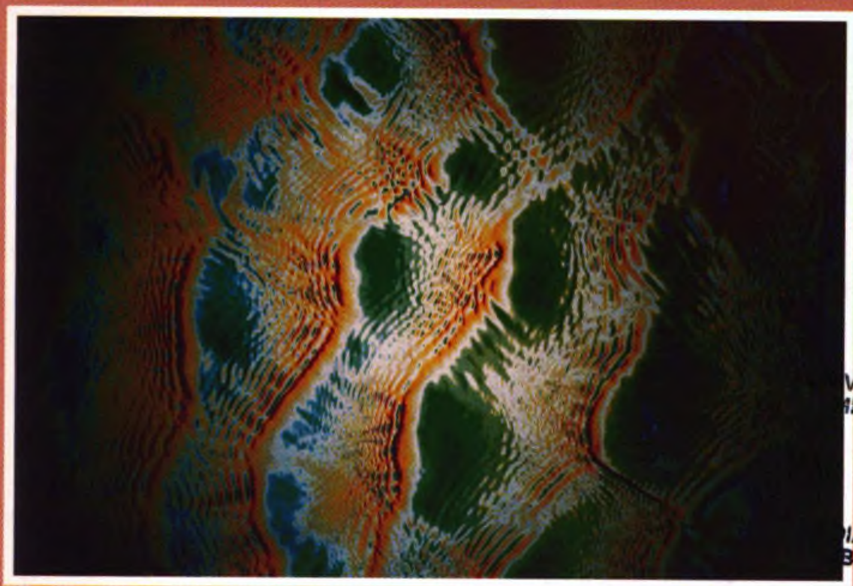

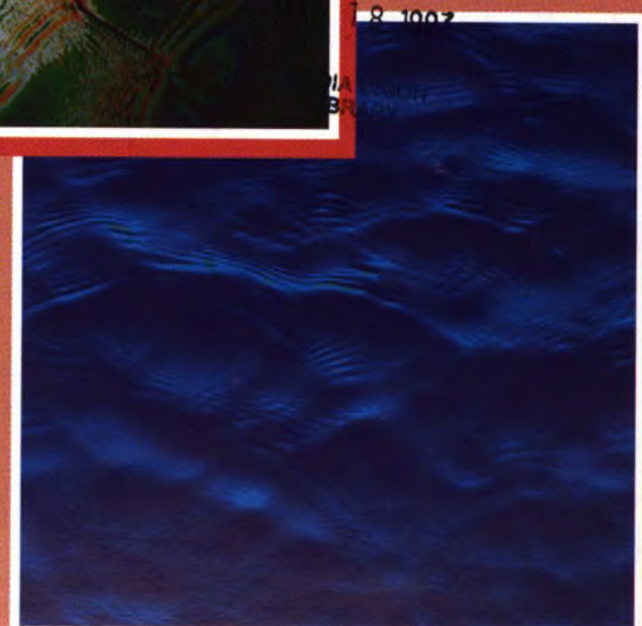

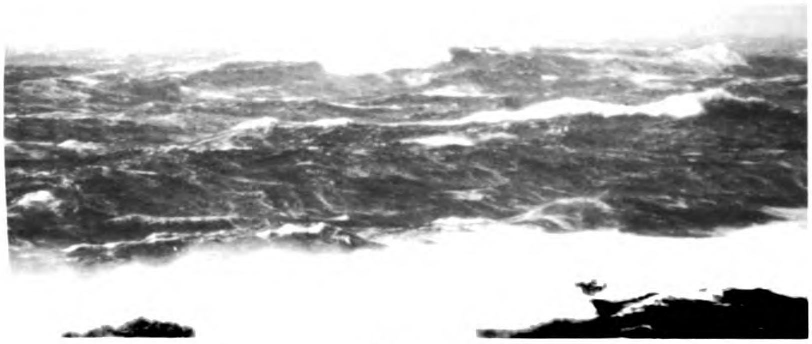

A

B

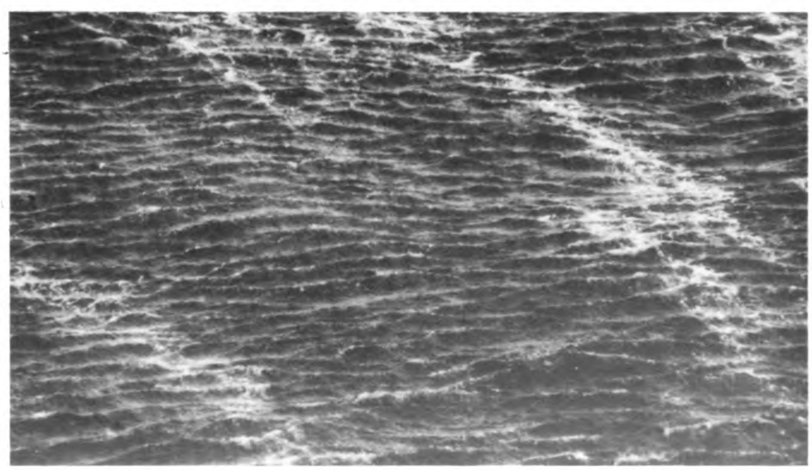

C

Examples of waves breaking from a storm in the North Atlantic in December 1993 in which the winds were gusting up to approximately 50-60 knots and wave heights of up to 12-15m were reported. a: Large scale breaking waves. b: Smaller-scale waves breaking on longer waves, c: Short strongly wind-forced breaking waves. (Photographs by E. Terrill and W. K. Melville, Scripps Institute of Oceanography)

Naval Research Reviews

Office of Naval Research
Three/1996
Vol XLVIII

This *Naval Research Reviews* on the topic of nonlinear ocean waves is published in two companion issues, Two/1996 (pages 1-28) and Three/1996 (pages 29-72). The introduction which puts the six articles into context and provides an historical perspective appears at the beginning of Two/1996.

Articles

Departments

About the Cover

(Top) An image from the Marseilles, France wind/wave facility of short gravity-capillary waves generated under wind conditions of 6.3 m/s and 5 m fetch. Wind forcing is left to right with yellow and red colors indicating wind slope in wind direction and green and blue indicating wave slope in the cross-wind direction. Cusp-shaped bores are seen to generatic short parasitic capillary waves in the direction of propagation that are thought according to current models to produce regions of high vorticity. Citation: Jaehne, B. And K. Riemer, "Two-dimensional wave number spectra of small scale water surface waves," J. Geophysical Research, v95, 11531-11546.

(Bottom) A model by Michalel Milder for the generation of short waves under constant wind forcing produced this similar image. The model incorporates gravity-capillary wave interations through a surface wave Hamiltonian approach. Citation: Milder, D.M., "An improved formalism for wave scattering from rough surfaces," J. Acoustical Society of America, v89, 529-541.

Naval Research Reviews publishes articles about research conducted by the laboratories and contractors of the Office of Naval Research and describes important naval experimental activities. Manuscripts submitted for publication, correspondence concerning prospective articles, and changes of address, should be directed to Code OPARI, Office of Naval Research, Arlington, VA 22217-5000. Requests for subscriptions should be directed to the Superintendent of Documents, U.S. Government Printing Office, Washington, DC 20403. *Naval Research Reviews* is published from appropriated funds by authority of the Office of Naval Research in accordance with Navy Publications and Printing Regulations. NAVSO P-35.

2D Complex Wavelets for Analysis of Unsteady, Wind-Generated Surface Waves

G.R.Spedding
Departments of Aerospace & Mechanical Engineering
University of Southern California Los Angeles, CA

Abstract

Wavelets and their transforms (WT) have numerous and diverse applications, and almost as many shapes and sizes. This article concentrates solely on their utility as a quantitative measure of spatially-localised spectral amplitudes for *2D* data analysis. The physical problem concerns the time-dependent growth of wind- driven surface waves, starting from a flat surface. Although the problem lacks the full complexity of real ocean conditions, it is argued that because it is precisely defined, a combined experimental and theoretical program can advance our physical understanding, that may itself be projected onto field data. Certainly, the advent of nonlinearity in the wavefield is marked by intermittency and *3D* structure, and the WT is an appropriate basis for analysis. The wind-wave problem will be used as an example where the simultaneous, quantitative measurement of amplitude and phase modulations in an unsteady wave field leads to estimates of quantities such as the local dispersion relation that cannot easily be measured otherwise. Furthermore, the WT-derived results can be combined with simple analytical models to measure quantities that are both of great interest to the oceanographer, and that have traditionally been difficult to estimate. Finally, suggestions are made for future work and take a surprising direction.

What is the problem?

Why study small-scale wind waves?

For the purposes of this article, small-scale waves are those having wavelengths in the centimeter range. Both gravitational and surface tension effects are significant and so the physical problem is an interesting balance between the two. From a practical point of view, there are two reasons for interest. Capillary-gravity (*cg*) waves are the wave-like disturbances that first grow when a calm water surface is disturbed by wind. Later in time, the energy- containing scales are much larger, but at any instant, it is through smaller-scale motions such as *cg* waves that the instantaneous surface response mediates the fluxes of momentum and energy between the atmosphere and ocean. The second practical motivation is that remote sensing devices such as SAR are sensitive to scattering of electromagnetic radiation primarily in the shorter wavelengths characterised by *cg* waves. It is only by modulation of the shorter wavelengths that larger scale features are observable. Generally it is sufficient to model this effect as a 'roughness', but statistical roughness models and predictions will not behave realistically unless they are based on sound physical principles. As we shall see later, the *cg* wavefield can be extremely complex in structure, and further understanding leads inevitably to studies that fall squarely into the 'Nonlinear Dynamics' theme of this issue.

Why study the unsteady problem?

It is a mild understatement to observe that fluctuations of the local wind stress (in both space and time) occur over the ocean surface. While steady-state response models may work satisfactorily in some statistical sense, the transient response and physical understanding of how one state changes to another, together with the possible interactions between a time-varying component with another stationary one, are still of great interest. Furthermore, while the linearised models predict the initial stages of the surface response quite well, they cannot predict the subsequent evolution of low wavenumber (long wavelength) modes, *3D* pattern instabilities, and wave-wave interactions that follow. In other words, there still is a problem, and it has not yet been solved.

There is a second, more abstract, line of reasoning that also supports such a line of enquiry. One of the principal achievements of nonlinear dynamical systems theory has been to demonstrate how complex phenomena can be generated by simple, deterministic systems, with few degrees of freedom. Hopes have been raised that tasks of apparently daunting complexity may yet yield to analytical, predictive methods. In a similar vein, starting from the very evident fact that the real sea surface state is extremely complicated, one searches for the simplest possible model that can nevertheless exhibit sufficiently rich dynamics that it can account for the most important physical mechanisms.

Starting from scratch, we require a system that: (i) is clearly defined; (ii) can be modeled analytically, or numerically; (iii) can be tested experimentally, and (iv) can be generalised to situations of practical interest. Condition (iv) is rarely satisfied unless (ii) and (iii) involve a degree of understanding based on physical principles, and the failure of empirical matching of model parameters and coefficients when applied outside of the domain for which they have been carefully tuned is a rather familiar problem in oceanography.

The spectrum of analytical models for the air-water interface is bounded on the one hand by small amplitude, two-dimensional solutions of the Rayleigh equation for steady mean flows with boundaries at $x = \pm\infty$. Correspondingly, the Blasius solution to the incompressible, flat- plate boundary-layer equations for a specified origin in x gives the fetch-limited result. Between the two limiting cases, we are interested in the time-dependent problem, in the absence of external boundaries.

One might question the relevance of laminar model flows when the ocean applications are almost always turbulent, in both fluids. However, in the initial transient for a wind profile starting from rest, even if the flow itself is not perfectly laminar, the laminar instability modes could still be predominant in selecting the most energetic wave modes. In this respect, the laboratory experiment, incorporating some degree of turbulence in the growing profiles, provides a bridge between model and reality.

Why bother with laboratory experiments?

In the previous article, Norden Huang has considered the general applicability of wave-tank experiments to real ocean conditions. It is worth reiterating the basic philosophy behind our laboratory work and its relation to the overall problem outlined in the previous paragraphs. In contrast to field data, it is only in the relatively controlled conditions of the laboratory that parameters can be varied at will, independently, and repeatedly. It is not necessarily significant that conditions do not exactly match those of the open ocean, because the experiments can still provide non-trivial tests of analytical or conceptual models that are themselves of use over a broader range of parameters. The support or refutation of such models can still provide information about their ability to predict events in the real world. If and when the model fails, it can be extended or thrown away; in either event, the conditions under which it fails are now known

In the remainder of this article, a closely-linked theoretical and experimental research program will be described, where wavelet analysis will be used as a tool for identifying current limitations and pointing to future requirements.

The contribution of wavelet-based methods

Wavelets as atomic units

At the time of writing, there are 11 texts on wavelets in our university bookstore, and some are quite good. For a concise and readable introduction, it is hard to beat the *Algorithms and Applications* book by Meyer[1]. A more comprehensive and mathematical overview is presented in the introductory volume of the series on wavelets edited by Chui[2], and geophysical applications of varying quality can be found in a later volume[3] in the same series. Farge[4] has written a fine review on wavelets and turbulence, and further collections of theoretical advances and applications are accumulating.[5-7]

One of the great strengths of the field is in the mathematical depth and rigour of much of the derivation and analysis, which has revealed connections with hitherto unrelated techniques, from Littlewood-Paley analysis of the 1930's to modern quadrature mirror signal processing algorithms and spline functional analysis. Nevertheless, a zero-th order degree of sophistication in understanding wavelet-based signal analysis will suffice for our purposes. On this level, wavelets are simple oscillatory functions that have compact support, and thus can be used for local space-scale decompositions. The original function, f(x) (or f(t)), is expanded as a function of an additional scale variable, a

$$f(x) \rightarrow \mathcal{F}(a,x). \qquad (1)$$

The decomposition is effected by a convolution of f(x) with multiple copies of a single wavelet function, $\psi(x)$, that are systematically shifted and dilated to cover a range of characteristic scales, a, and positions, b

Provided certain admissibility criteria are met $\psi(x)$ must have finite energy, zero mean...consult refs.(1,2,4)), then the choice of $\psi(x)$ is somewhat arbitrary. It is possible to make the strong assertion that the physical world is much more likely to be composed of collections of wavelet-type, compactly supported functions, rather than, say, infinitely- extended oscillatory functions as in Fourier series. It follows that it is only reasonable to decompose real world observations (and computations) onto such atomic units. Farge[4], for example, draws attention to the fact that a decomposition of a complex fluid flow into its elementary coherent structures (if such an object exists), is better approximated by a functional base with compact support than the usual Fourier base. Alternatively, one might search for basis functions whose properties are extracted from the data, or from known solutions to the particular governing equations. There will likely be future progress in this direction, but it is in fact unnecessary to adhere so strictly to the atomic construct.

Wavelets as tools for quantitative description

The keyword, of course, is 'construct', and one is free to construct a wavelet, or any other, basis to represent the world in many different ways. For example, one of the principal advantages of Fourier representations is the considerable mathematical convenience in computation of PDE's, having little or nothing to do with any implied physical basis. Similarly, provided one is aware of the properties of the decomposition and its role in determining (even distorting) the interpretation of the world, one can still use a wavelet basis for descriptive purposes. This is not all the same thing as stating that wavelet-atoms actually exist, or that they have any special dynamical significance. Hence, we simply state the following:

1. *The objective is to make quantitative measurements and interpretations of local energy densities in a 2D, time-varying surface wave field.*

2. *The most straightforward way to do this is through continuous, complex-valued wavelets.*

The definition of the wavelet transform (WT), described in words above, can be statd more precisely:

$$\mathcal{F}(a,b) = \int f(x).\psi^{*}\left(\frac{x-b}{a}\right)dx. \qquad (2)$$

The transform is a sum of the convolution of the translates and dilates of $\psi^{*}(x)$ with f(x) (the * denotes the complex

Figure 1.

Is the world composed of wavepackets like this? The Morlet wavelet is a smooth, continuous wave function, modulated by a Gaussian envelope. Real and imaginary parts are shown in continuous and dotted lines. Whether or not it is a true atomic unit of the physical world, it can still be a convenient function basis for general description.

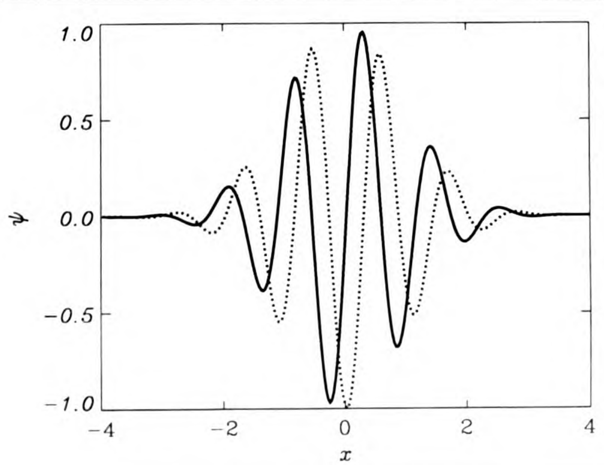

Figure 2.

The 2D wavelet function Arc is defined most conveniently in Fourier space where for a given scale, a, it can be seen to interrogate an arc that covers all wavevectors of magnitude |k|, regardless of their orientation.

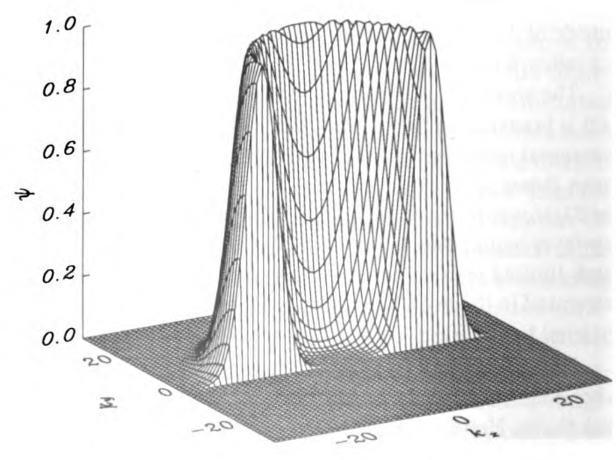

conjugate). In one dimension, a useful choice of $\psi(x)$ is the Morlet[8] wavelet.

$$\psi(x) = e^{ik_0 x} \cdot e^{-(|x|^2/2)}. \tag{3}$$

As Figure 1 demonstrates, it is a complex-valued function, and the $\pi/2$ phase shift between real and imaginary parts allows the modulus of its coefficients to be free from oscillations due to changes in phase in an otherwise constant amplitude signal. The wavelet phase indicates the phase in the instantaneous frequency, or wavenumber, associated with a particular scale, a.

k_0 is constant (typically) so there is a fixed number of cycles in an analysing wavelet, regardless of a. Consequently, the spatial resolution improves with increasing wavenumber, or decreasing a. The way in which it does so varies automatically with a, and the balance between resolution in wavenumber space and in physical space is in some sense an optimum for the Morlet wavelet, within the overall constraints of Heisenberg's uncertainty principle.

The WT conserves energy, and a form of the Parseval relation can be written,

$$\int_{-\infty}^{\infty} |f(x)|^2\, dx = \frac{1}{C_\psi}\int_{+0}^{\infty}\int_{-\infty}^{\infty} |\mathcal{F}(a,b)|\cdot|\mathcal{F}^*(a,b)|\, \frac{da\,db}{a^2}, \tag{4}$$

Figure 3.

The time evolution of alongwind surface slope following a change in mean wind, U_{10}, from 0m/s to 6.8m/s. The change in wind speed is approximately linear over 5 seconds. The time series shown here begins at t = 5.3s, i.e. after U_{10} has reached its steady value. The field of view in each image is approximately 14 x 11.5 cm.

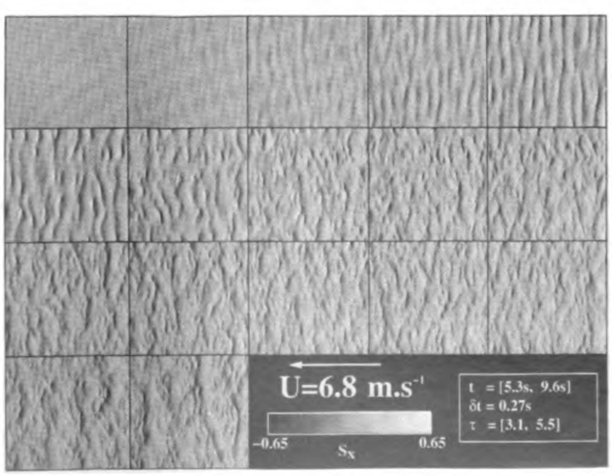

where $C\psi$ is a normalisation constant that depends on the form of $\psi(x)$. The right hand side is an integral of a function that is proportional to the spatial distribution of energy density per unit scale. It is possible to integrate contributions from all x to arrive at a global power spectrum,

Figure 4.

Experimentally-measured initial exponential growth rate, β, vs. wavenumber, k_x (symbols connected by solid lines), for U_{10} from 2.8 - 10.2 m/s. The solid symbols are from experiments of Kawai, and the dashed lines are results from Kawai's Orr-Sommerfeld model integration for parameters that closely matched those experiments (U_{10} is given in brackets). At moderate windspeeds, the agreement is good, but is very sensitive to assumptions about how the boundary layer grows, and so remains somewhat empirical, because there is no analytical model for the boundary layer growth. A simple diffusion model does not work at all, and a pessimist might well argue that the agreement simply signifies that both parties have done similar experiments. As selected, the best match occurs at moderate windspeeds, but the extremes are not so well covered.

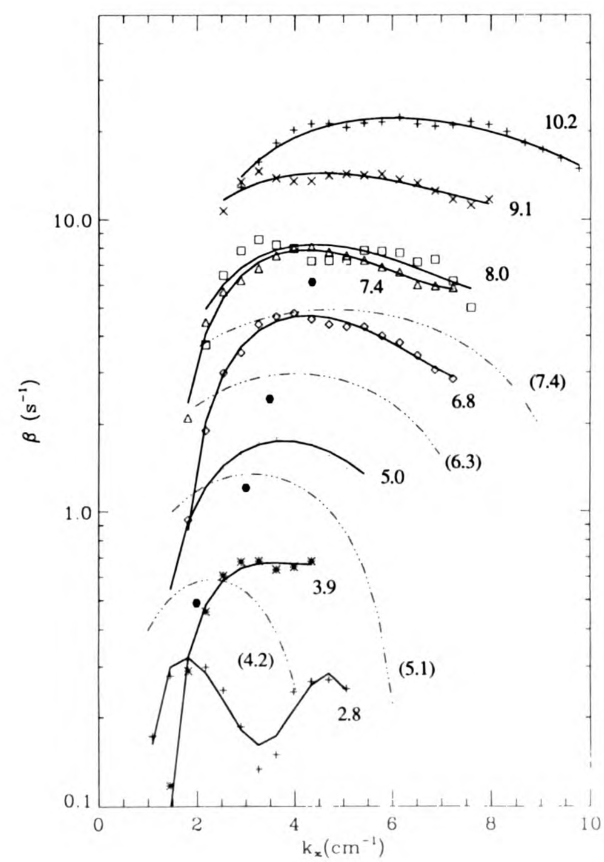

$$E(a) = \frac{1}{C_\psi}\int_{-\infty}^{\infty} |\mathcal{F}(a,b)|^2 \frac{db}{a^2}. \tag{5}$$

$E(a)$ is a Gaussian-smoothed version of a power spectrum that could equally well have been obtained from Fourier transforms. Of course, in this case we are not obliged to perform the summation over x, and the point is to note that the energy densities are precise, quantitative measures of localised spectral components (provided that there are no artifacts from the mutual interaction of overlapping, non-orthogonal wavelet coefficients).

The extension to two dimensions of this basic approach is fairly straightforward and details can be found in ref. 9. As before, we require a complex wavelet function, and for real-valued signals (*2D* surface slope measurements, for example) it is sufficient to cover the half-plane in wavenumber space. Now that $\psi = \psi(x,y)$, the wavelet can be designed so that it can be either directional-specific, or non-directional. A non-directional wavelet responds equally to wavevectors at all angular orientations, and in two dimensions such a function covers an arc that sweeps through 180° in $\{k_x, k_y\}$ (Fig. 2).

Arc and its close relatives form the core of the data analysis, giving a measure of instantaneous, wavenumber energy densities and wave phase as a function of $\{x,y\}$.

An integrated analytical/ experimental program

Theory

The time-varying solution for perturbations to the interface between two viscous fluids with specified shear-flow profiles can be solved numerically by integrating coupled Orr- Sommerfeld equations for air and water. Both Valenzuela[10] and Kawai[11] have done that, two decades or so ago. Exponential growth rates for *cg* waves were predicted (and measured, in the case of Kawai) and compared reasonably well with microwave backscatter measurements of Larson & Wright.[12] This body of work represents, still, the state-of-the-art in the numerical analysis of the linearised problem.

The stability of piecewise linear shear profiles in air and water was recently examined by Caponi *et al.*[13] One can take their steady-state model and integrate forwards in time by allowing a boundary layer thickness to grow, thus generating a quasi-steady solution. The sensitivity of the solution to the assumed growth of the boundary layer thickness will tell us much about the behaviour of the numerical solutions, and the directions for further improvements.

Figure 5.

The modulus of the wavelet transform, $|WT|_{a0}$, at the initially most amplified scale (k_0=4.0 rad/cm, λ_0=1.6cm). The colour bar mapping is constant over the series, which covers the exponential growth, saturation, and decline in energy densities around this scale. Although the wavenumber and growth rates are quite well predicted, as described in Figure 4, the distribution is far from uniform $\{x,y\}$.

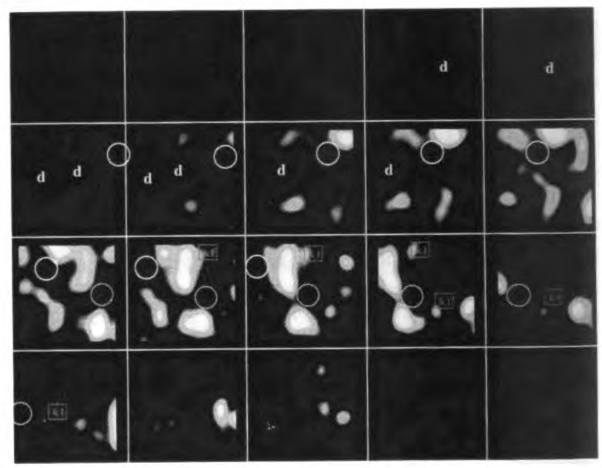

Experiment

Experimentally, we investigate the growth of disturbances on an initially calm water surface when the wind starts from rest, and at sufficient fetch so that upstream boundary conditions can be ignored (at least in the water). The configuration is a reasonably close experimental approximation of the theoretical approaches discussed above.

The measurements are made with a modified form of the Imaging Slope Gauge (originally described by Jähne & Riemer[14]), which uses surface refraction of intensity-graduated incident light to derive the instantaneous along- or cross-wind slope over the field of view. $s_x(x,y,t)$ or $s_y(x,y,t)$ can be reconstructed according to the direction of the light intensity gradient. The surface slope, $s_{x,y}$, is directly related to the wave energy, and the WT time series, $\tilde{s}_{x,y}(x,y,a,t)$ contains information about the local energy densities, and about the local wavenumber- frequency relation. Model predictions can thus be carefully checked. For the first time, the unsteady, local dispersion relation can be measured, and related to the *2D*, instantaneous structure of the wavefield.

Matching the two

Neither existing models, nor practicable experiments can provide complete and generalisable information about the time-varying, *3D*, wave and velocity fields. It will emerge that the theoretical models are very sensitive to, and experiments mostly ignorant of, the detailed shape and time-evolution of the water and air boundary layers. However, in combination, mutual consistency checks and judicious matching of empirical data with analytical relations can lead to new methods for measuring and/or inferring the values of physical variables (surface stress, boundary layer height), not only from laboratory data, but also from remote sensing measurements. Two examples of this kind of reasoning will be given. In both cases, the glue that holds the pieces together is the *Arc* wavelet transform.

The time evolution of capillary-gravity waves

The surface wave growth for a mean wind, $U_{10} = 6.8$ m/s (measured at 10 cm above the calm water surface) is shown in Figure 3. The time series proceeds from left to right, top to bottom, and is for wind forcing from the right. The dimensionless time $\tau = U_{10}t/X$, where X is the fetch, ranges from 3 to 5.5, so the upstream origin is always felt in the air flow, even at the early times. The group velocity of the initial water waves, however, is much smaller. At 50 cm/s, for example, 24 seconds are required to travel the fetch distance of 12m.

It is clear that, even at early times, the observed wavefield is never perfectly two-dimensional. The grey-scale encoding of the slope magnitude gives the initial disturbances an organ-pipe appearance, but they always have Y-shaped 'defects', or 'dislocations', where successive waves become entangled. In fact, it was the presence of the defect patterns that first drew our attention to the wind-wave problem, as we wondered whether there may be similarities with other defect structures in fluid turbulence.[15-17]

Even though the waves are not perfectly two-dimensional, calculation of the global power spectral densities and their rate of change with time shows that the most amplified wavenumbers, and their initial exponential growth rates, can be quite well predicted by linear theory (Figure 4). That is true for the first five images (the top row) in Figure 3. During the course of about 1.25s, the initially most-amplified disturbances have reached their maximum amplitude, and in the top right panel, the waves look as two-dimensional as they ever will be. Shortly afterwards, the surface patterns become much more complicated as the initial modes saturate and further growth occurs in sidebands of both higher and lower wavenumber. By the end of the series longer wavelength disturbances predominate. A convincing physical explanation for this well-known phenomenon has never been given. Note, however, that it does appear to be a duration-limited event, since information propagated by water waves from upstream boundaries will not yet have reached the measurement window. Further insights can be derived from wavelet analysis.

Figure 6.

$|WT|_{a_{-1}}$ for same time series as Figure 5. Maximum growth of the lower wavenumber mode (k_{-1} = 2.2 rad/cm, λ_{-1} = 2.9 cm) occurs around the middle of the third row, just when the peak of the initially most amplified mode in Figure 5 begins to saturate and decay. The boxes marked 'k_1' are located at the energy density peaks and correlate well with peaks at the higher wavenumber mode (k_1=7.9 rad/cm, λ_0=0.8 cm; not shown).

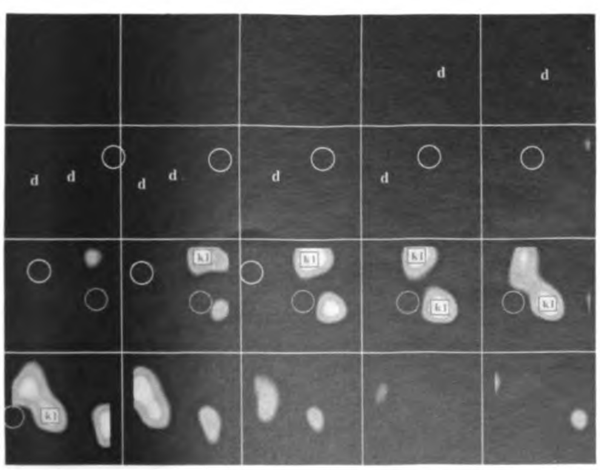

Wavelet-based analysis

Local energy density distributions

The remarks concerning the global evolution of instability modes are based on Fourier analysis. The *2D* Fourier transform can provide a perfectly good description of the average properties of the surface slope, and has very good spectral resolution. Having identified the wavenumbers of interest, it is now possible to use the localised properties of the wavelet transform to relate the spectral densities to the structure of the wavefield.

The spatial distribution of growth of the initially most amplified mode at U_{10} = 6.8 m/s can be seen in Figure 5. The energy density distributions are quite patchy, and remain so. By analogy with defects in mixing layers, where the defects are the sites for the first (and subsequent) subharmonic transitions, it is reasonable to ask whether the globally-measurable sideband instabilities are located at, or near, defect sites in the surface wave field. The open circles denote the location of defects, identified by eye in the equivalent time series of surface slope. Again, by analogy with the mixing layer results, the local energy density at the fundamental scale, a_0, would be a minimum here, while the sideband modes would peak at the same location. At first glance, the circles do seem to be consistently beside, rather than on, the highest energy densities in a_0. However, Figure 6, which is the same plot for the lower

Figure 7.

The waveprint. The sign of the phase of the WT at a_0 allows defect sites to be located with little ambiguity, enabling automated identification and tracking algorithms to work reliably.

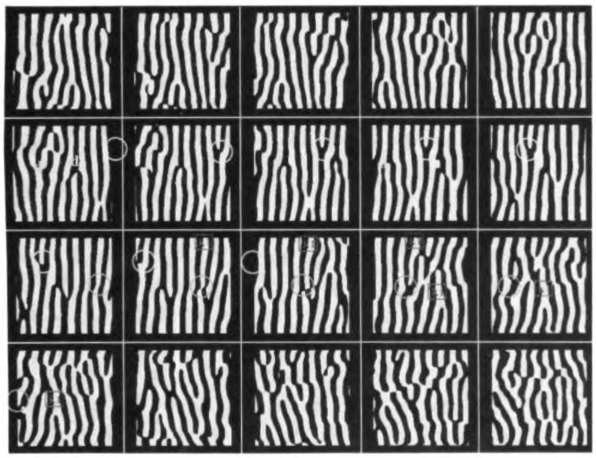

wavenumber sideband, a_{-1}, shows that the circles are *not* associated with local maxima at this scale. It can also be found that the other sideband, characterised by wavelet scales a_1, is correlated quite well with maxima in a_{-1}, and so, also not with a_0. The high and low wavenumber modes correlate well with each other, but only weakly with minima in the initial mode. Initially, the defects do not appear to play a significant rôle in the development of sidebands. Although one cannot expect spatial correlations to be maintained in a dispersive wavefield, the variation in phase speed with wavenumber is rather weak at this particular range of scales, and the wave pattern defects or dislocations do not appear to be involved in the growth of sidebands.

Pattern defects and the waveprint

The correlation of pattern defects with various postulated transitions and instabilities could be made more precise if a reliable method for identifying the defect sites were available, and we recently found one.

Recall that it is specifically defects at a particular scale that we would like to investigate, and the WT can be employed as a kind of filter so that only contributions from this scale are counted. Images such as Figures 5 & 6 are clearly of no use, but the phase of the WT is. Figure 7 is a binarised image of the phase of the WT at scale a_0. Not only can one confirm the defect locations that were originally identified by eye (circles), but it is also possible to follow their time evolution. None of the defect topologies in the circles remains fixed over time; instead connections with preceding or following waves are initiated and broken. In a similar spirit to the description of fluid flows by critical points,[18] the wavefield topology can be characterised by the type and location of its defects, together with the distribution of the highest amplitude wavelet coefficients. Just as fingerprints can be categorised by their defects, so the wavefield can be described by its waveprint. One can look for particular defect structures in an appropriate analytical model, and Paul Newton at USC has made a start in describing a new family of defect solutions to the nonlinear Schrödinger equation.[19]

Figure 8.

How to calculate the instantaneous, local dispersion relation $\omega(k, x, y)$ from a time series of complex wavelet transforms. Given the surface slope distribution, $s_x(x,y)$ (top row), at two closely-spaced times, t_1, t_2, the wavelet transform of each can be separated into modulus and phase components (rows 2 & 3). For all scales having significant energy densities, the flow field that maps the isophase lines from their position at t_1 to their position at t_2 can be computed from an optical flow technique. Note that frequencies higher than the apparent Nyquist limit can be found because the structure in the phase field allows large displacements to be computed in a global optimisation solution. Finally, only measurements that occur where $|WT| > |WT|_{thresh}$ are retained.

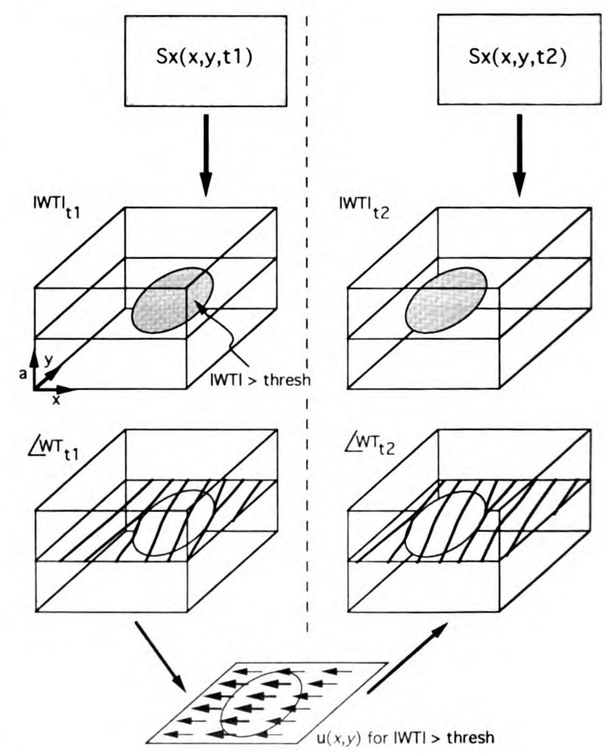

Combined analytical/ experimental models for prediction

Estimation of local dispersion relation

The WT gives a measure of the spatially-localised energy densities as a function of wavenumber, and since the measurements are also well-resolved in time, the local frequencies can be calculated from $\omega = \partial\phi / \partial t$. This is possible because the complex WT also gives the instantaneous phase distribution, $\phi(x,y)$, associated with each scale (as shown in the waveprint). Figure 8 shows how the calculation proceeds. The flowfield, u(x,y), that maps $\phi(x,y,t_1)$ to $\phi(x,y,t_2)$ at all energetic scales, a (associated with physical wavenumber, k), is used to compute the local frequency as.

$$\vec{\omega}(x,y) = |\, k\,(x,y)| \vec{u}(x,y). \qquad (6)$$

There is no comparable time-dependent, 2D theory that predicts such a detailed dispersion relation, but values over all {x,y} can be collected together and compared. Figure 9 is an example, where the solid curves have been drawn over an arbitrary range of k from the result of Caponi *et al*[13] for the intrinsic $\omega(k)$ of small perturbations on a surface between two piecewise linear shear profiles. The experimental results differ from the theoretical curves, which is not altogether surprising since the wavelengths (and frequencies) that actually have the largest amplification rate in practice will depend on the time history of the growth in boundary layer thickness, $D(t)$, and surface drift velocity, $U_w(t)$. In fact, from the difference between the measured $\omega(k)$ and the solid curve, either the surface drift or the boundary layer thickness can be inferred. This is an example of a combined experimental/theoretical modeling for simultaneous measurement of a variable whose estimation could be of great importance in the field.

Estimation of surface stress from lab, or field data

Now let us suppose that U_w is known (from existing experimental data or field measurements. The maximum slope thickness, D, can be written as the ratio of the mean wind, U, to the gradient of $\partial U/\partial y$ at the water surface

$$D = \frac{U}{\left|\frac{\partial U}{\partial y}\right|_{y=0}} \qquad (7)$$

The friction velocity, u_*, is a measure of the wind stress exerted at the water surface, which also varies with $\partial U/\partial y$:

$$u_*^2 = \frac{\tau_{y=0}}{\rho} = \frac{\mu}{\rho}\left|\frac{\partial U}{\partial y}\right|_{y=0} \qquad (8)$$

where μ and ρ are the air viscosity and density, respectively. Combining the two expressions, the friction velocity can be related to D,

$$u_*^2 = \frac{\nu U}{D}, \qquad (9)$$

where $\nu = \mu/\rho$ is the kinematic viscosity. An estimate of D is therefore equivalent to an estimate of the friction velocity. To see how this relationship can be incorporated into the overall

Figure 9.

An example comparison of measured $\omega(k)$ with theoretical predictions in solid curves. Each symbol marks the average value of the collection of points at a particular wavenumber where |WT| exceeds a threshold value. Each spatial location contributes a dot, and the collection of dots forms a vertical line whose length shows the variation in measured ω for a given k. The first two timesteps cover the regime that is adequately described by linear theory. After τ=4.95, the scatter increases and by τ=5.23, there are no wavelet coefficients that exceed the threshold value at the originally most-amplified wavenumber.

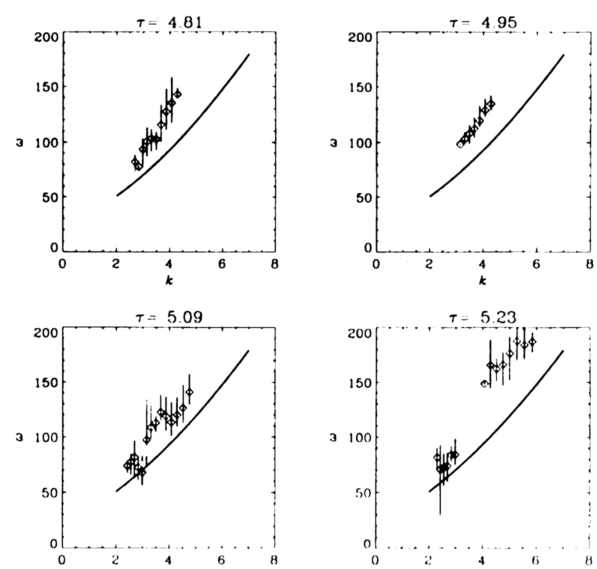

framework, see Figure 10. At the heart of the scheme is the combined theoretical model for $\omega(k)$ together with experimental measurements of the same quantity. Given a measured dispersion relation, and a selection criterion for choosing one particular curve, such as the maximum amplification rate, then the difference between measured and predicted $\omega(k)$ curves can be attributed to the surface drift current, U_w. The corrected ratio of the water and air velocities are returned to the theoretical model, and upon convergence, a predicted value of $D=D_p$ can be used to measure u_*. It is noteworthy that the measurements do not have to come from laboratory data. In principle, a time series of SAR images could provide the same information, because the WT can give estimates of $\omega(k)$ from these data also.

The two examples above demonstrate how the newly-acquired ability to measure instantaneous amplitude and phase information for local spectral components can lead to novel and potentially powerful measurement techniques that have application in both laboratory and ocean data.

Figure 10.

A flow diagram for the procedure for estimating wind friction velocity from measured inputs, ω, k and U_a. The inputs may come from either laboratory or field data. The subscripts w and a refer to quantities in water and air, respectively, and subscripts m and p identify measured and predicted values.

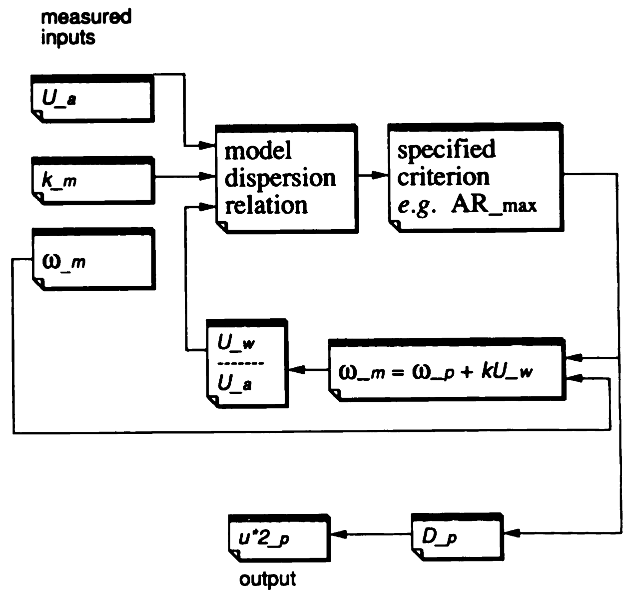

Concluding remarks

The wind-wave startup problem has been explored as an example of the application of wavelet-based measurement and analysis techniques to unsteady, inhomogeneous data. It is the extension to these domains that brings us closer to realistic ocean conditions, and clearly into nonlinear regimes that have just begun to be investigated. The advanced measurement techniques have application to both laboratory and field conditions.

With regard to the particular wind-wave problem, it is obvious that the wavefield is always quite complex in structure, but the dynamical significance of the complexity is not equally obvious. In attempting to distinguish between structure that is due to intrinsic instability of the water surface deformation, or that merely reflects imprecision in specification of the initial forcing, we need a smaller-scale, more easily controllable experiment. The form of the mean wind profile, and its time history, must be specified. Then, an experimental program with modulations in both along- and cross-wind directions to generate particular instability modes would be a wind-forced equivalent of existing systematic investigations of liquid surface instabilities.[20-23]

Paradoxically, the conclusion that future experiments ought to be in smaller, more precisely- controlled containers, moves still further from true-blue oceanography, where Reynolds numbers are large, and many simultaneous processes compete and/or interact with each other. Recalling the introduction however, it is likely that the basic instabilities and physical mechanisms will only be isolated and identified with a more selective, and precisely specified experiment. We hope to report on the results of similar experiments in the future.

Acknowledgments

It is a pleasure to thank my friends and colleagues, Paul Newton, and especially, Fred Browand, for their expert counsel during the course of this research. We thank also our co-collaborators Norden Huang and Steve Long, at NASA Goddard/Wallops Island, and Bernd Jähne and Jochen Klinke at Scripps Institute. All of us thank Lou Goodman and Mike Shlesinger for their support, and also Alan Brandt, who helped initiate the research while he was at ONR.

Biography

Geoff Spedding received B.Sc. and Ph.D. degrees in Zoology at the University of Bristol, England in 1978 and 1981. His doctoral work concerned the aerodynamics of bird flight. He moved to USC to work on mechanical modeling of insect wings, which became a project on unsteady separated flows on delta wings. Working in the Geophysical Fluid Dynamics Laboratory (http://ae-www.usc.edu/rsg/gfd/gfd_index.html) with Tony Maxworthy, it was inevitable that GFD would become an interest. He is currently a Research Associate Professor, and has research projects involving signal and image processing (wavelet analysis, DPIV motion estimation, grid interpolation), GFD (wind-generated surface waves, decaying turbulence and submerged wakes in stable density gradients) and animal aerodynamics (theoretical models of flapping animal flight, function of nonplanar insect wing surfaces). Address: Department of Aerospace Engineering, University of Southern California, Los Angeles, CA 90089-1191, e-mail: geoff@ostrich.usc.edu

References

1. Meyer Y 1993 Wavelets: *Algorithms and Applications*. SIAM, Philadelphia

2. Chui CK 1992 Wavelet Analysis and its Applications. (ed. CK Chui) Volume 1: *An Introduction to Wavelets*. Academic Press, New York.

3. Geogiou EF & Kumar P 1994 Wavelet Analysis and its Applications. (ed. CK Chui) Volume 4: *Wavelets in Geophysics*. Academic Press, New York.

4. Farge M 1992 Wavelet transforms and their applications to turbulence. *Ann. Rev. Fluid Mech.* **24**, 395-457.

5. Ruskai M, Beylkin G, Coifman R, Daubechies I, Mallat S, Meyer Y & Raphael L 1992 *Wavelets and their Applications*. Jones & Bartlett, Boston.

6. Benedetto JJ & Frazier MW 1994 *Wavelets: Mathematics and Applications*. CRC Press, London.

7. Chui CK, Montefusco L & Puccio L 1994 Wavelet Analysis and its Applications. (ed. CK Chui) Volume 5. Academic Press, New York.

8. Grossmann A & Morlet J 1984 Decomposition of Hardy functions into square integrable wavelets of constant shape. *SIAM J. Math. Anal.* **15**, 723-736.

9. Dallard T & Spedding GR 1993 2D wavelet transforms: generalisation of the Hardy space and application to experimental studies. *Eur. J. Mech. B/Fluids* **12**, 107-134.

10. Valenzuela GR 1976 The growth of gravity-capillary waves in a coupled shear flow. *J. Fluid Mech.* **76**, 229-250.

11. Kawai S 1979 Generation of initial wavelets by instability of a coupled shear flow and their evolution to wind waves. *J. Fluid Mech.* **93**, 661-703.

12. Larson TR & Wright JW 1975 Wind-generated gravity-capillary waves: laboratory measurements of temporal growth rates using microwave backscatter. *J. Fluid Mech.* **70**, 417-436.

13. Caponi EA, Caponi MZ, Saffman PG & Yuen HC 1992 A simple model for the effect of water shear on the generation of waves by wind. *Proc. R. Soc. Lond.* A **438**, 95-101.

14. Jähne B & Riemer KS 1990 Two-dimensional wave number spectra of small-scale water surface waves. *J. Geophys. Res.* **95**, 11531-11546.

15. Dallard T & Browand FK 1993 The growth of large scales at defect sites in the plane mixing layer. *J. Fluid Mech.* **247**, 339-368.

16. Coullet P, Gil L & Lega J 1989 A form of turbulence associated with defects. *Physica D* **37**, 91-103.

17. Spedding GR, Browand FK, Huang NE & Long SR 1993 A 2D complex wavelet analysis of an unsteady wind-generated surface wave field. *Dy. Atmos. Ocean* **20**, 55-77.

18. Perry AE, Lim TT & Chong MS 1980 The instantaneous velocity fields of coherent structures in coflowing jets and wakes. *J. Fluid Mech.* **101**, 243-256.

19. Newton PK & O'Connor M 1996 Scaling Laws at Nonlinear Schrsdinger Defect Sites. *Phys. Rev. E.* (to appear)

20. Henderson D & Hammack J 1987 Experiments on ripple instabilities. Part 1. Resonant triads. *J. Fluid Mech.* **184**, 15-41.

21. Perlin M, Henderson D & Hammack J 1990 Experiments on ripple instabilities. Part 2. Selective amplification of resonant triads. *J. Fluid Mech.* **219**, 51-80.

22. Perlin M & Hammack J 1991 Experiments on ripple instabilities. Part 3. Resonant quartets of the Benjamin-Feir type. *J. Fluid Mech.* **229**, 229-268.

23. Liu J, Schneider JB & Gollub JP 1995 Three-dimensional instabilities of film flows. *Phys Fluids* **7**, 55-67.

Profiles in Science

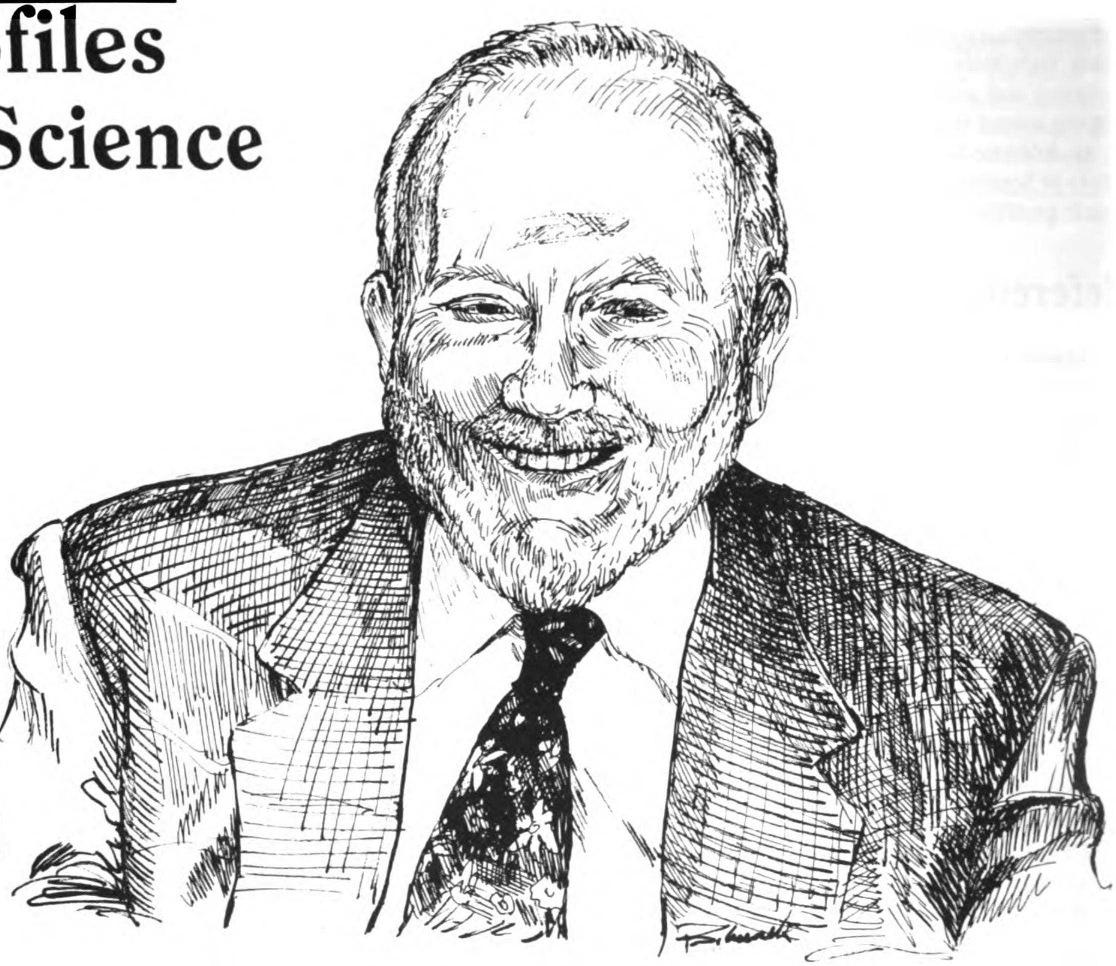

Marshall Tulin

Marshall Tulin has been a major contributor to Navy ocean wave research for over 45 years. He served as a research leader at the Navy's David Taylor Model Basin from 1950 to 1954 and was a Research Scientist and Office of Naval Research Scientific Liaison Officer to London from 1954 until 1959. He was the Founder of Hydronautics, Inc. and served at various times as Vice-President, Technical Director, Chief Executive Officer and Board Chairman during the years 1959 through 1982. Since 1982, he has been an ONR Principal Investigaor at the University of California, Santa Barbara (UCSB) where he is Professor and Director, Ocean Engineering Laboratory, and continues to train new generations of students in ocean wave dynamics.

Professor Tulin's research has profoundly influenced our quantitative understanding of the onset and mechanisms of wave breaking, the role of wave groups in wave breaking, and the essential role of breaking as the cause of downshifting. He has continuously applied his research results to important Navy problems: most recently combining wave theory, radar measurements and scattering theory to produce a new model for wave energy directional distribution as it is effected by shoreline topography. The work explains previous anomalies as well as when and how peak waves travel on rays nearly parallel to the shoreline under certain circumstances and off of the wind direction. The results led to a predictive model that is very useful to coastal operations. He has also played a crucial role in the interpretation of radar remote sensing of the ocean background at low grazing angles.

Professor Tulin has been the recipient of numerous honors and awards including the U.S. Navy Meritorious Civilian Service Award in 1957 and again in 1994. He is a Member of the National Academy of Engineering.

Nearshore Observations of Nonlinear Ocean Surface Gravity Waves

Steve Elgar, School of Electrical Engineering and Computer Science, Washington State University, Pullman, WA
T.H.C. Herbers, Department of Oceanography, Naval Postgraduate School, Monterey, CA
R.T. Guza, Center for Coastal Studies, University of California at San Diego, La Jolla, CA

Introduction

Wind-generated surface gravity waves (figure 1, frequencies between approximately 0.05 and 0.5 Hz) are the energy source for nearshore fluid motions having a range of spatial and temporal scales. In shallow water (depths less than about 10 m) near-resonant nonlinear interactions result in significant cross-spectral energy transfers and strong evolution of wave shapes over distances of only a few wavelengths. As waves shoal, energy is nonlinearly transferred from the wind waves (about 0.1 Hz in figure 2) that dominate the wave field outside the surf zone (736 cm depth in figure 2) to both higher and lower frequencies. Sum interactions excite phase coupled motions at relatively high frequencies, resulting in the sharp crests and steep forward faces characteristic of near-breaking waves and bores (153 cm depth in figure 2). Difference interactions are believed to generate lower frequency (nominally 0.005-0.05 Hz) infragravity waves ("surf beat") which dominate current and sea-surface elevation fluctuations in the swash zone where wave breaking has substantially reduced the wind-wave energy (0 cm depth in figure 2).

These nonlinearly excited motions may play a central role in nearshore sediment transport. Phase coupling between wind waves and higher frequency harmonics causes asymmetrical near-bottom horizontal velocities and accelerations widely believed important to cross-shore sediment transport (eg, Bowen 1980, Bailard 1981, Bailard & Inman 1981, Hanes & Huntley 1986, Doering & Bowen 1988, Elgar et al. 1988). Strong infragravity motions are the dominant sediment suspension mechanism in the inner surf zone during storms (eg, Holman et al. 1978, Wright et al. 1982, Beach & Sternberg 1988).

The nonlinear evolution of ocean surface gravity waves propagating through the nearshore to the beach observed at several field sites will be reviewed here. First, sum interactions that transfer energy to higher frequency motions will be considered, followed by a discussion of the excitation of lower frequency motions by difference interactions.

Nonlinear Sum Interactions

Well seaward of the beach, in depths comparable to or greater than the wavelength ($|\mathbf{k}|h > 1$, where $\mathbf{k}$ is a typical wavenumber and h the water depth), ocean waves are characterized by strong frequency dispersion and broad directional distributions. Changes in the wave field caused by gradual variations in the water depth are well described by linear propagation models (eg, Longuet-Higgins 1957, Collins 1972, Berkhoff 1972, Radder 1979, Le Me'haute' & Wang 1982, Kirby 1986a, 1986b, Kirby & Dalrymple 1986, Panchang et al. 1990). At second order in weakly nonlinear theory (Phillips 1960, Hasselmann 1962), forced secondary motions arise

Figure 1.

Two breaking waves (in about 2 and 5 m depths) at the U.S. Army Corps of Engineers' Field Research Facility pier near Duck, NC. The deck is about 7.5 m above mean sea level. The surf zone extends more than 1 km offshore. (From Elgar et al. 1995.)

which can be interpreted as small, but significant corrections to the underlying linear wave field. For example, interactions between directionally opposing wind waves excite long wavelength secondary waves that dominate high frequency (eg, greater than about twice the spectral peak frequency) pressure fluctuations at the seafloor (figure 3), which in turn drive seafloor microseisms (Longuet-Higgins 1950). Energy levels and wavenumbers of high frequency, secondary pressure fluctuations observed at the seafloor in relatively deep water ($|\mathbf{k}|h \approx 3$) are consistent with the predictions of weakly nonlinear theory (Herbers & Guza 1991, 1992, 1994). Resonances between quartets of waves occur at the next higher order, resulting in slow cross-spectral energy transfers. Although nonlinear energy exchanges are small on wavelength scales, the frequency-directional spectrum can be substantially modified over hundreds of wavelengths (Phillips 1960, Hasselmann 1962, and others). As the depth decreases ($|\mathbf{k}|h < 1$), secondary wave effects are enhanced and skewed wave shapes develop with sharp crests and broad, flat troughs. The nonlinearity of wave-induced pressures and orbital velocities is readily detected in intermediate water depths and accurately predicted by second-order nonlinear theory for a wide range of wave conditions (Herbers et al. 1992).

In very shallow water ($|\mathbf{k}|h < 1$, typically near or within the surf zone), waves are approximately nondispersive, directional distributions are narrow (owing to refraction during shoaling), and strong nonlinearities drive relatively rapid spectral evolution. Models based on the nondispersive, nonlinear shallow water equations for unidirectional waves (Hibberd & Peregrine 1979) predict many important features of bore propagation and runup (Kobayashi et al. 1989, Raubenheimer et al. 1995, and references therein).

The transition region between dispersive deep and nondispersive shallow water regimes is the shoaling region, characterized by weakening dispersion, narrowing directional spread, and substantial nonlinearity. Waves propagating through the shoaling region evolve significantly in several (rather than hundreds of) wavelengths, with nonlinear interactions driving phase-locked harmonics that cause the pitched-forward shape characteristic of nearly breaking and broken waves (Freilich & Guza 1984, Elgar & Guza 1985a, 1985b, Elgar et al. 1990, Kaihatu & Kirby 1995, and many others). In particular, nonlinear interactions occur among triads of waves with frequencies f_i and wavenumbers $\mathbf{k}_i$ obeying the interaction rules (Armstrong et al. 1962, Bretherton 1964):

$$f_1 + f_2 - f_3 = 0 \quad (1a)$$

$$\mathbf{k}_1 + \mathbf{k}_2 - \mathbf{k}_3 = 0 \quad (1b)$$

For sum interactions, the primary wave components 1 and 2 each obey the lowest-order (linear) dispersion relation

Figure 1A.

Elevation versus time (arbitrary units) of a sawtooth wave shape (dashed line, skewness = 0, asymmetry = 2.3) and its Hilbert transform (solid line, skewness = 2.3 and asymmetry = 0.). The time series have identical power and bicoherence spectra, but different biphases. (From Elgar et al. 1990.)

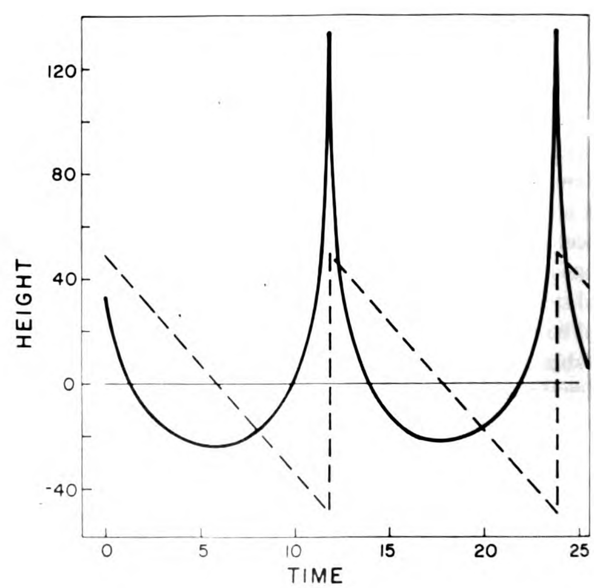

Figure 2.

Near-bottom pressure time series (top) and power spectra (bottom) well outside the surf zone (736 cm depth), in the breaking region (153 cm depth), and on the beach face (swash excursions, 0 cm depth).

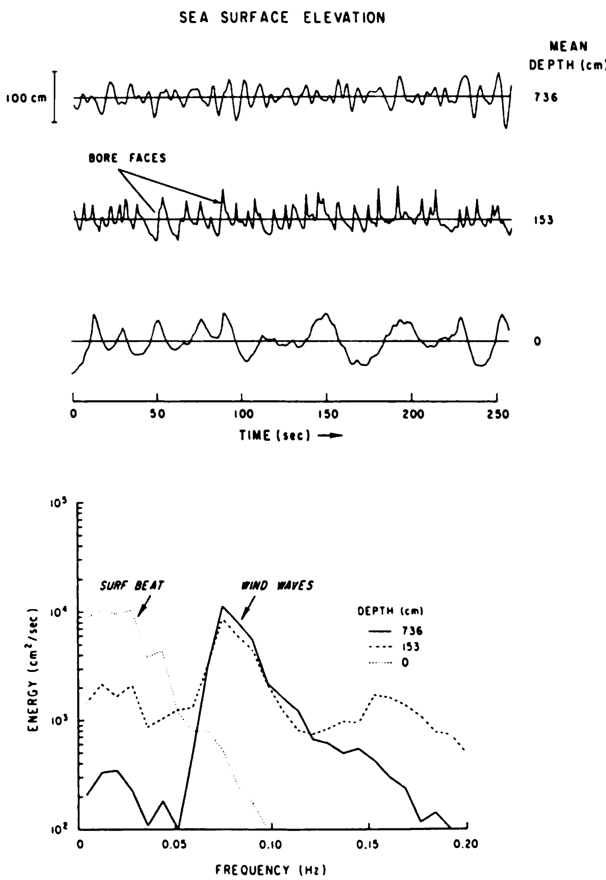

$$(2\pi f)^2 = g\,|\boldsymbol{k}|\tanh(|\boldsymbol{k}|h) \qquad \text{(1c)}$$

and force a new component 3 with the sum frequency and the vector-sum wavenumber. In the nonresonant case where component 3 does not obey (1*c*), there is a small energy transfer to secondary "bound waves" (Phillips 1960, Hasselmann 1962). On the other hand, in the resonant case where the sum component exactly satisfies the dispersion relation (1*c*), continuous energy transfers occur between the three modes and component 3 grows at the expense of components 1 and 2. Armstrong et al. (1962) showed that significant energy also can be exchanged between the three waves of the triad if the sum component nearly satisfies the dispersion relation ("near-resonant" interactions).

The evolution of a wave field dominated by nearly normally incident, narrow-band swell (peak frequency f = 0.06 *Hz*, significant wave height H_s = 60 cm in 9 m depth) observed on a monotonically sloping (slope ≈ 0.05) beach near Santa Barbara, CA is shown in figures 4-6. In 9 m water depth (figure 4a) there is a small spectral peak at the first harmonic (f = 0.12 *Hz*) of the swell. As the waves shoal, the power in the first and higher harmonic (f ~ 0.12, 0.18, 0.24, 0.30 *Hz*) peaks increases (figures 4b-d, upper panels). The growth of these harmonics is not predicted by any linear theory, but is accurately modeled (Freilich & Guza 1984) by near-resonant sum interactions based on the nonlinear Boussinesq equations (Peregrine 1967).

Figure 3.

Bottom-pressure spectral density versus frequency at 4-min intervals (times and line types are given in the legend) immediately following a sudden shift in wind direction. Note the large increases in secondary-pressure spectral levels at double-wind wave frequencies (about 0.35-0.70 Hz). The pressure gage was located on the seafloor in 13 m depth near Duck, NC. Pressure spectral have been converted to equivalent spectra of vertical water column displacements. (From Herbers & Guza 1994.)

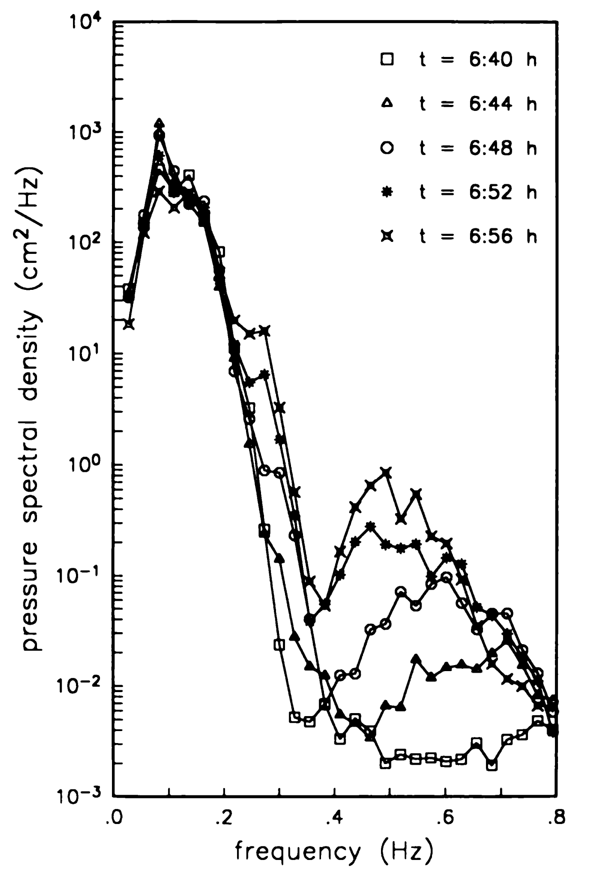

Figure 4.

Power spectra (cm^2/Hz) and contours of bicoherence for narrow band swell. The power spectra (bars indicate 95% confidence levels) are immediately above the corresponding bicoherence spectra. Contours indicate quadratic coupling among the triad of waves with frequencies f_1, f_2, and $f_1 + f_2$. The minimum bicoherence contour level is b = 0.1, with additional contours every 0.05. There are 310 degrees of freedom and the 95% significance level for zero bicoherence is b = 0.14. Depths are (a) h = 9.0, (b) 3.9, (c) 2.7, and (d) 1.3 m. The data were observed on Leadbetter Beach, Santa Barbara, CA. (From Elgar & Guza 1985b.)

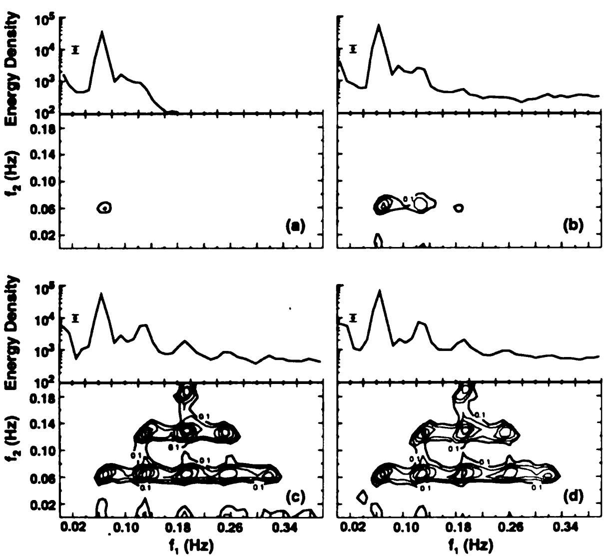

Figure 5.

Biphase versus depth for selected frequency pairs (with nonzero bicoherence) for the narrow band swell. Asterisk, (f, f); circle, (f, 2f); plus, (f, 3f); triangle, (2f, 2f); diamond, (2f, 3f), where f = 0.06 Hz corresponds to the power-spectral-peak frequency. (From Elgar & Guza 1985b.)

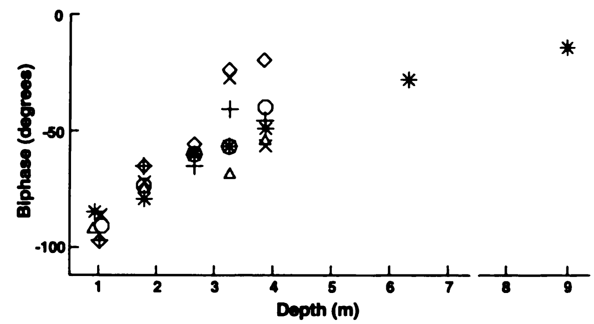

Below each power spectrum in figure 4 is the corresponding bicoherence spectrum, $b(f_1, f_2)$ which detects phase coupling between triads of waves with frequencies f_1, f_2 and $f_1 + f_2$ (see Appendix for details on bispectral analysis). If the 3 waves in the triad are independent of each other, as would occur in a Gaussian (linear) sea, $b^2(f_1, f_2) = 0$. On the other hand, $b^2(f_1, f_2) = 1.0$ if all the energy with frequency $f_1 + f_2$ is phase coupled to the waves with frequencies f_1 and f_2. In a natural wave field interactions occur across a broad range of frequencies so that $0 < b^2(f_1, f_2) < 1$, and $b(f_1, f_2)$ can be interpreted as a relative measure of nonlinear coupling between waves with frequencies f_1, f_2, and $f_1 + f_2$.

At the seaward edge of the shoaling region (water depth h = 9 m, figure 4a) there is weak coupling between the swell ($f_1 = f_2 = 0.06\ Hz$) and its harmonic ($f_3 = 0.12\ Hz$). As the waves shoal, the excitation of phase-coupled harmonics is clearly visible in the bicoherence spectra. In 4 m depth (figure 4b), the bicoherence indicates enhanced coupling between the swell and its first two harmonics (triads with frequencies (0.06, 0.06, 0.12) and (0.06, 0.12, 0.18) Hz). In 1.3 m depth (figure 4d) the unbroken swell is coupled to its first through fifth harmonics (contours with $f_2 = 0.06\ Hz$), and the harmonic with frequency 0.12 Hz is coupled to even higher harmonics (contours with $f_2 \approx 0.12\ Hz$). Although these bispectral calculations indicate which frequencies are nonlinearly coupled, and not the direction of energy flow (ie, which frequencies are receiving energy), the sequence of power spectra (figure 4) shows that energy is predominantly transferred to higher frequencies.

Along with increased bicoherence during shoaling (figure 4), there is substantial biphase evolution (figure 5). The biphase is a statistical measure of the shapes of the waves (see Appendix). For example, the biphase of a Stokes wave (a wave with tall, narrow crests and broad, flat toughs) is zero, while the biphase of a sawtooth is $-\pi/2$. The bicoherence and biphase evolution (figures 4 and 5) show that Stokes-like waves in 9 m depth (the biphase of the most energetic triad $f_1 = f_2 = 0.06\ Hz$ is ≈ 0) evolved to sawtoothed-shaped waves with steep front faces and gently sloping rear faces (biphases of all triads are $\approx -\pi/2$) in 1 m depth. These observed shape changes are also evident in the time series that show wave profiles evolving from slightly peaked shapes in 9 m depth to the pitched-forward shapes of nearly breaking waves in shallower water (figure 6).

The observed evolution of a locally generated broadband wave field (figure 7, also with H_s= 60 cm in 9 m depth) is markedly different. The power spectra and bispectra are featureless, showing no evidence of the prominent harmonic peaks observed with the narrow-band swell (compare figures 4 and 7). The bicoherences evolved from near-zero values in 9 m depth to low (but statistically significant) values spread over the entire wind-wave frequency range in 0.9 m depth

Figure 6.

Sea-surface elevation versus time for a short section (about 90 s) of the narrow bank swell data set. (a) h = 8.7, (b) 2.9, (c) 2.4, and (d) 1.0 m. (From Elgar & Guza 1985b.)

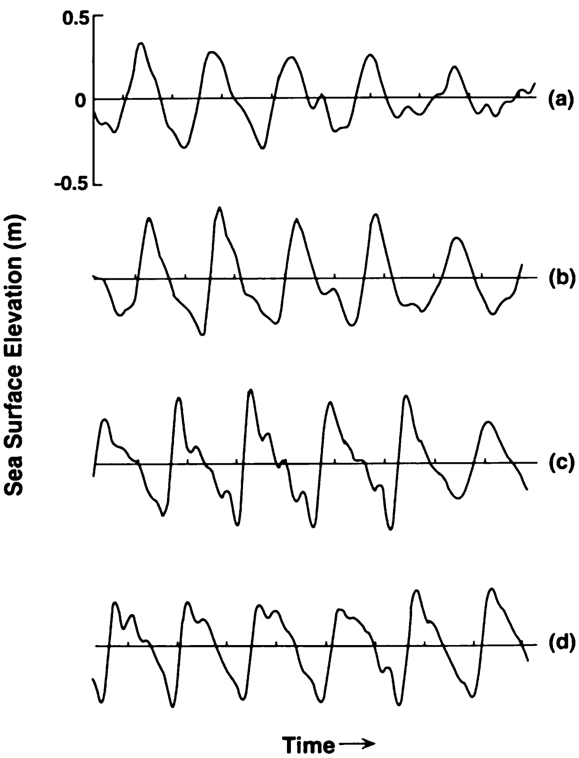

(figure 7). Strong nonlinearity occurs as in the narrow swell case, but it is masked in the power spectra because the interactions are distributed over a wide range of frequencies.

Despite the radically different evolution of power and bicoherence spectra for the narrow and broadband wave fields, the evolution of biphase and wave shape is similar. In both cases, the biphases evolved from near zero in 9 m depth to $-\pi/2$ just before the waves broke, and the waves had steep front faces and flat rear slopes in very shallow water (compare figures 6 and 8).

A bulk statistical characterization of an average wave shape is provided by third moments of the sea-surface elevation time series. Skewness, the normalized third moment of the time series, indicates the degree of peakedness of the waves (eg, the lack of symmetry about a horizontal plane caused by differences between the shapes of wave crests and troughs). Asymmetry, another normalized third moment of the time series, indicates the degree of pitched-forwardness of the waves (eg, the lack of symmetry about a vertical plane caused by differences in the shapes of leading and trailing wave faces). Skewness and asymmetry are equal to normalized sums of the real and imaginary parts of the bispectrum, respectively. Thus, bispectra (see Appendix) indicate which frequency triads contribute to total third moments (skewness and asymmetry) of measured time series, similar to the way in which the standard frequency spectrum shows which frequencies contribute to the total second moment (variance). Although the bicoherence spectra for the two wave fields are quite different, the evolution of the bulk wave skewness and asymmetry is similar. Skewness is relatively low in 9 m depth (figure 9), increases to a maximum in about 2 m depth, and then decreases to near zero in shallower water. Asymmetry is near zero in 9 m depth, but increases as the waves shoal.

The observations shown in figures 1-9 were obtained on monotonically and moderately sloping beaches where wave breaking limits the spatial extent over which nondissipative, nonlinear evolution can occur. Significantly stronger nonlinear evolution was observed over a nearly horizontal (flat), 2 m deep beach section extending about 80 m from the toe of the foreshore seaward to a small sand bar (figure 10) during the recent ONR funded Duck94 nearshore field experiment. In particular, nearly breaking ("feathering" of the wave crests was observed) narrow-band swell (H_s = 80 cm) that was strongly pitched forward near the sand bar (asymmetry ≈ 0.5 near

Figure 7.

Power spectra and contours of bicoherence for a broadband wave field, in a format identical to figure 3. Depths are (a) h = 8.7, (b) 3.5, (c) 2.2, and (d) 0.9 m. The increase in high frequency energy (f > 0.2 Hz) is an artifact of not correcting the deepest measurement (made with a bottom-mounted pressure gage) for depth attenuation. (From Elgar & Guza 1985b.)

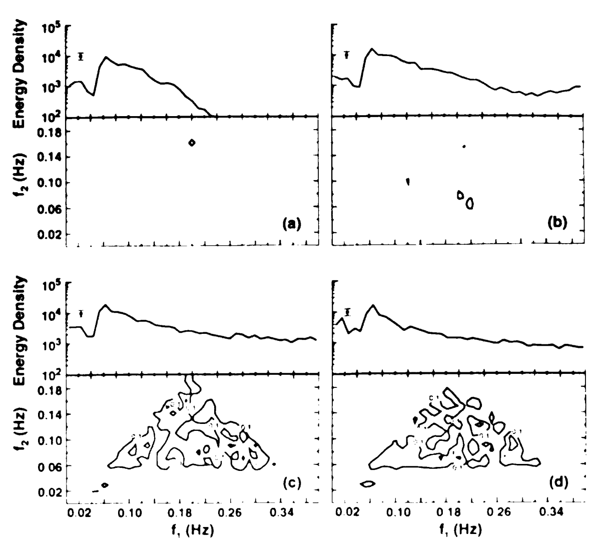

cross-shore coordinate x = 280 m, figure 10) became unpitched during further propagation in constant depth. At the shoreward end of the flat section (x = 180 m, figure 10) the asymmetry was nearly zero (and even slightly negative), in contrast to moderately sloping beaches where strong positive asymmetry (pitched forwardness) is a precursor to breaking and waves remain pitched forward across the surf zone. The changes in the wave spectrum during propagation across the flat section of the beach were dramatic (figure 11). In 8 m depth (cross-shore coordinate x = 884 m in figure 10) the dominant wave period was about 11 s (figure 11). In 2 m depth, at the seaward edge of the flat section (x = 240 m), small crests were beginning to emerge in the troughs of the 11 s swell. These resonantly excited waves continue to grow as the nonbreaking waves propagate over the flat beach section, and by its shoreward edge there are twice as many wave crests as offshore (compare figures 11a and 11c). Although the dramatic frequency doubling shown in figure 11 was rare because narrow-band swell occurred infrequently, nonbreaking waves with a range of spectral shapes had similar evolution of skewness and asymmetry over the flat beach section.

Figure 8.

Sea-surface elevation versus time for a short section (about 90 s) of the broadband wave field. (a) h = 8.4, (b) 2.5, (c) 1.9, and (d) 0.9 m. (From Elgar & Guza 1985b.)

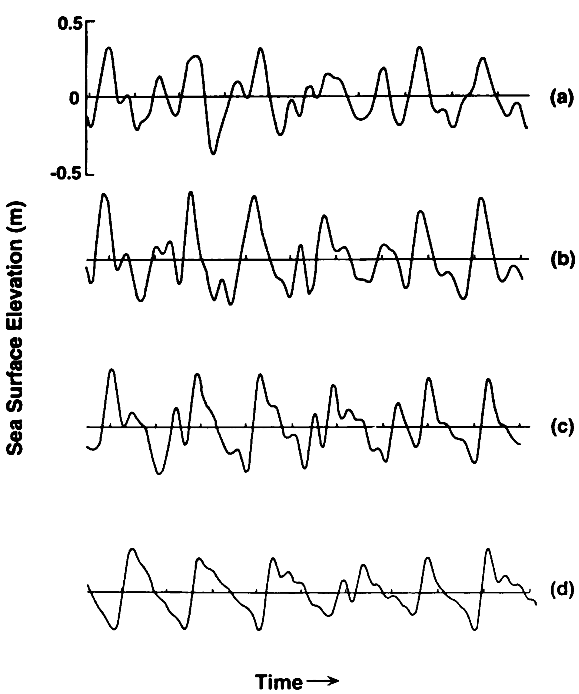

Figure 9.

Skewness and asymmetry versus depth. Asterisk, narrow band swell; circle, broadband wave field; solid curves are skewness and dashed curves are asymmetry. The data were band-pass filtered between 0.04 and 0.4 Hz. (From Elgar & Guza 1985b.)

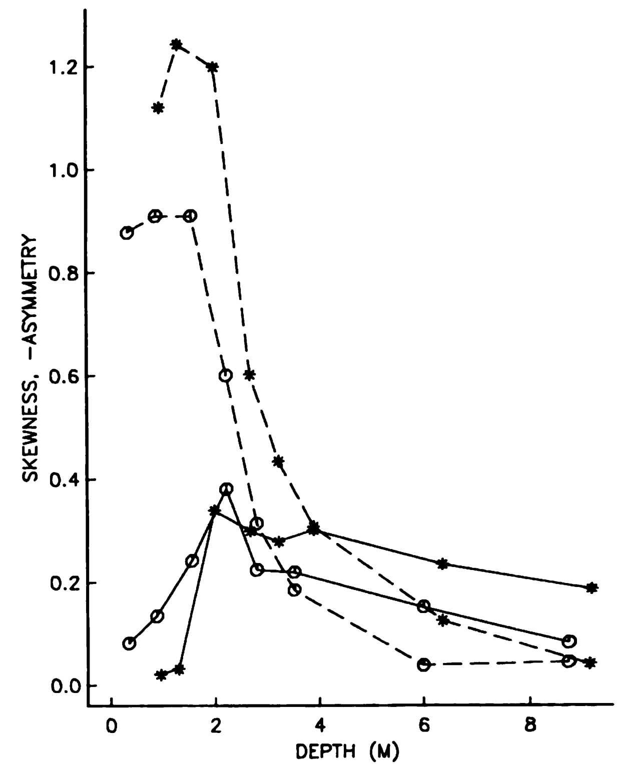

Nonlinear Difference Interactions

There is considerable interest in waves in the infragravity frequency band (0.005 < f < 0.05 Hz) on the beach and continental shelf. In addition to sometimes dominating wave runup at the shoreline (figure 2), infragravity waves can resonantly excite ocean structures and small harbors. Nonlinear difference frequency interactions between a pair of swell components with slightly different frequencies f and $f + \delta f$ drive an infragravity frequency (δf) secondary (forced) wave. The magnitude of this secondary wave, which is phase-locked to groups of swell, depends on the directional properties of the swell waves (Hasselmann 1962). Predictions of forced wave energy levels, based on weakly nonlinear theory and the frequency-directional spectrum of swell (estimated with a 24-element array of pressure sensors in 13 m depth near Duck, NC) are consistently lower than observed infragravity levels (figure

Figure 10.

(a) Cross-shore transect of instruments deployed near Duck, NC. The symbols represent colocated sonar altimeters (to determine the bottom location), bottom-mounted pressure sensors, and bidirectional current meters. (b) Skewness and asymmetry versus cross-shore location for the narrow band swell observed to undergo frequency doubling. Asterisks, skewness; squares, asymmetry. The data were band pass filtered between 0.05 and 0.3 Hz.

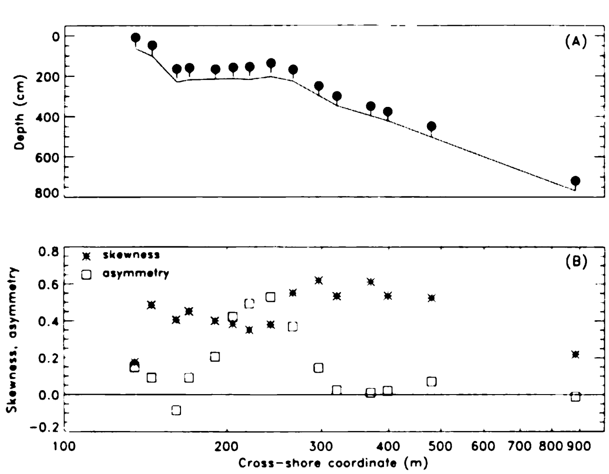

12a). The observed infragravity motions are a mixture of forced waves phase locked to the local groups of swell and freely propagating (uncoupled) waves. Using bispectral analysis to separate free from forced infragravity waves, Herbers et al. (1994) demonstrate that second-order nonlinear theory accurately predicts the observed forced infragravity energy levels (figure 12b). However, forced waves usually contribute only a small fraction of the total infragravity energy (0.1 to 30% at the 13 m depth Duck, NC site). Analysis of data from many shelf sites (figures 13 and 14) shows that free waves are usually the dominant infragravity motion on the shelf (Herbers et al. 1995b). However, the relative contribution of forced wave energy to the infragravity band is highly variable and generally increases with both increasing swell energy and decreasing depth (figure 14). During high energy conditions ($H_s > 4$ *m*) forced wave energy levels may exceed free wave levels even in 200 m depth (figure 14c).

Strong correlations between energy levels of infragravity waves and swell observed at all sites (figure 13) indicate that free infragravity waves are driven by swell, as suggested by Munk (1949) and Tucker (1950) nearly 50 years ago. However, the details of the infragravity wave generation process and the subsequent propagation of infragravity waves across the shelf are still poorly understood. Observed directional properties and cross-shore energy variations show that free infragravity waves are predominantly radiated from shore and refractively trapped on the shelf. Infragravity wave generation appears to be sensitive to the local beach bathymetry, whereas the refractive trapping depends on the regional shelf topography. The net result of this sensitivity is that free infragravity energy levels vary widely between sites in the same water depth with similar swell conditions (Herbers et al. 1995b).

Longuet-Higgins & Stewart (1962) suggested that while incident swell are dissipated by breaking in very shallow water, the associated forced secondary infragravity waves are somehow released as free waves and reflect from the beach. Consistent with this mechanism, infragravity motions in the surf zone have been shown to be phase coupled to groups of wind waves seaward of the breaking region (Guza et al. 1984, Elgar & Guza 1985b, List 1992). Additional support for the hypothesis of Longuet-Higgins and Stewart (1962) is provided by the observed strong dependence of the ratio of upcoast to downcoast directed infragravity wave energy fluxes on the same ratio in the swell frequency band (figure 15). Note however that the ratio of infragravity energy fluxes is usually much closer to 1 (ie, comparable upcoast and downcoast fluxes) than is the ratio of swell energy fluxes, suggesting that upcoast (or downcoast) propagating swell drives both upcoast and downcoast propagating infragravity waves. Herbers et al. (1995a) show that secondary infragravity waves (excited by difference interactions of swell) exhibit this unusual directional behavior,

Figure 11.

Sea-surface elevation versus time for the narrow-band, frequency-doubling swell. (a) cross-shore location x = 884, (b) x = 240 (the seaward edge of the flat section), and (c) x = 160 m (the shoreward edge of the flat section). There are twice as many wave crests at x = 160 than at x = 240 m. (d) Energy density versus frequency at the same locations.

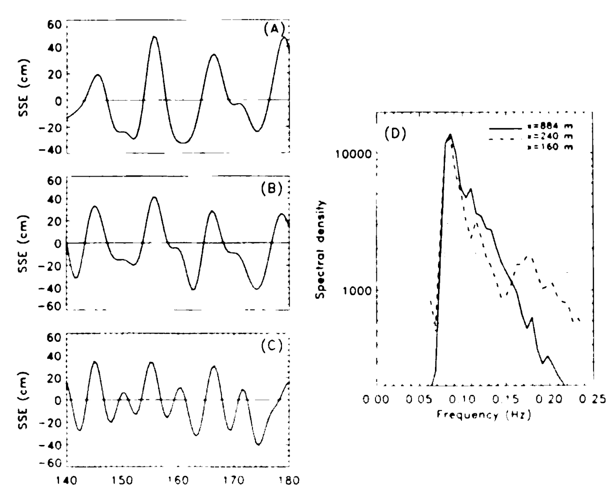

Figure 12.

(a) Predicted forced versus observed total (free plus forced) infragravity energy and (b) predicted versus observed forced infragravity energy in 13 m depth near Duck, NC. (From Herbers et al. 1994.)

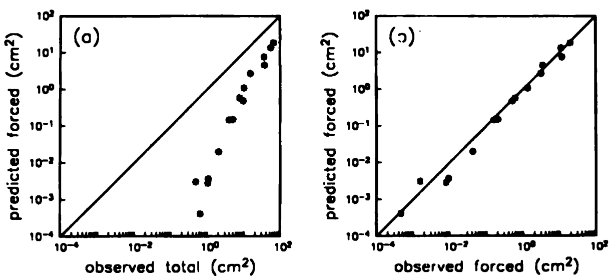

and that the observed up to downcoast infragravity energy flux ratio agrees well (figure 16) with predictions based on the hypothesis that forced secondary waves are released during the breaking process. Although further work is needed to assess the importance of wave breaking to infragravity wave generation and damping, these results lend strong support to the basic hypothesis that infragravity waves are driven by nonlinear difference interactions between pairs of swell components.

Summary

Near-resonant nonlinear triad interactions result in significant cross-spectral energy transfers and phase modifications to ocean surface gravity waves over distances of a few wavelengths in water depths less than about 10 m. As waves shoal, energy is nonlinearly transferred from wind waves (frequencies between about 0.05 and 0.2 Hz) that dominate the wave field outside the surf zone to both lower and higher frequencies. Nonlinear sum-frequency interactions among wind waves excite phase coupled motions at higher frequencies, resulting in the sharp crests and steep forward faces of near-breaking waves and bores. Nonlinear difference-frequency interactions generate lower frequency (nominally 0.005-0.05 Hz) infragravity waves which sometimes dominate current and sea-surface elevation fluctuations in the runup where wave breaking has substantially reduced the wind-wave energy.

Appendix: Bispectral Analysis

Since their introduction more than thirty years ago (Hasselmann et al. 1963), bispectral techniques, which isolate nonlinear interactions between the Fourier components of a time series, have been used to study many systems (see Nikias & Raghuveer 1987 and Elgar & Chandran 1993 for reviews).

Figure 13.

(top) Cross-shelf depth variations and pressure gage locations (asterisks) at several field sites (Chesapeake Light is off the Virginia coast; Duck is off the North Carolina Coast; Ventura, Redondo, and Santa Rosa are in the Southern California Bight; Harvest Platform is off the California coast near Pt. Conception; Oahu is off the Hawaii coast.) (center) Average spectral shapes (the average of spectra normalized by the variance in the range 0.0005-0.14 Hz). (bottom) Observed correlation between logarithms of spectral levels in narrow (0.0005 Hz wide) frequency bands with total swell energy (0.05 - 0.14 Hz) as a function of frequency. (From Herbers et al. 1995b.)

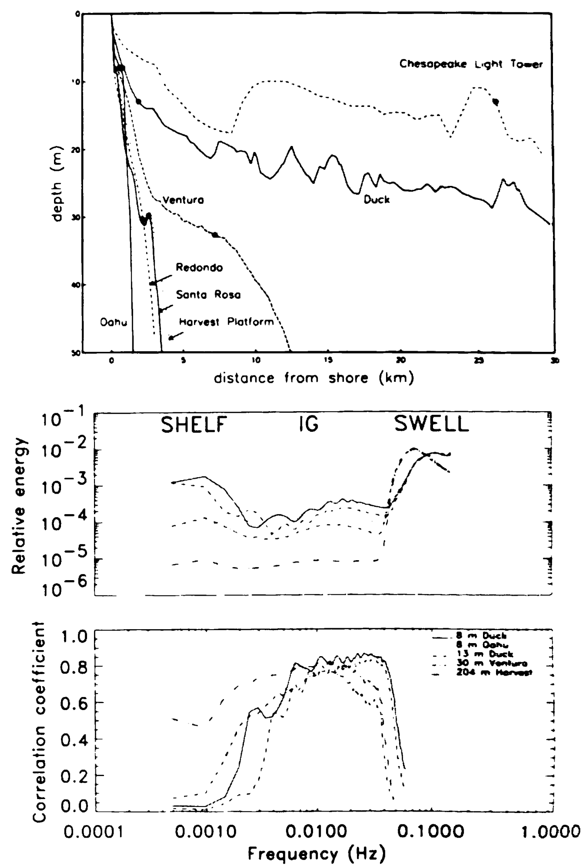

The discrete bispectrum, appropriate for discretely sampled data, is (Haubrich 1965, Kim & Powers 1979)

$$B(f_1, f_2) = E\,[A_{f_1} A_{f_2} A^*_{f_1+f_2}]\,. \qquad \text{(A1)}$$

where the A_{f_n} are complex Fourier coefficients at frequency f_n, the subscript n is a frequency (modal) index, asterisk indicates complex conjugation, and $E\,[\cdot]$ is the expected-value, or average, operator. Similarly, the power spectrum is defined here as

$$P(f)=\frac{1}{2}E\,[A_f A_f^*]\,. \tag{A2}$$

It is convenient to recast the bispectrum into its normalized magnitude and phase, called the squared bicoherence and biphase, given respectively by (Kim & Powers 1979)

$$b^2(f_1,f_2)=\frac{|B(f_1,f_2)|^2}{E[|A_{f_1}A_{f_2}|^2]E[|A_{f_1+f_2}|^2]}\,, \tag{A3}$$

Figure 14.

(a) Forced infragravity energy, (b) free infragravity energy, and (c) the ratio of forced to free infragravity energy versus swell energy. The data are from 8 m depth at Duck, NC (triangles, upper clouds), 30 m depth at Ventura, CA (asterisks, middle clouds), and 204 m depth at Harvest Platform, CA (squares, lower clouds). Least-squares-fit curves to the logarithms of the observed energies are denoted by solid lines. Dashed lines labeled 1 and 2 indicate a linear and quadratic dependence, respectively. (From Herbers et al. 1995b.)

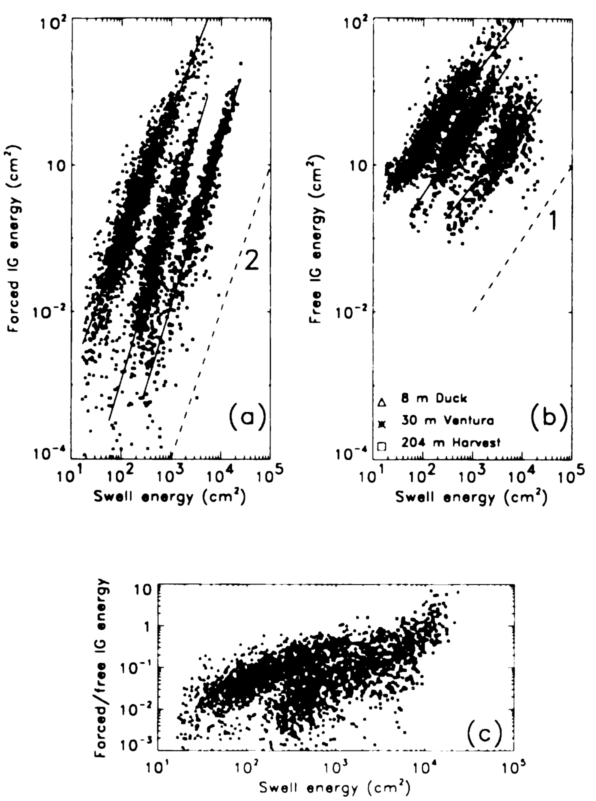

Figure 15.

The ratio $F^{IG}_{up}/F^{IG}_{down}$ of the upcoast to the downcoast component of the alongshore energy flux in the infragravity frequency band versus the analogous flux ratio $F^{swell}_{up}/F^{swell}_{down}$ in the swell frequency band. The dashed line corresponds to equal ratios. The data were observed in 13 m depth near Duck, NC. (From Herbers et al. 1995a.)

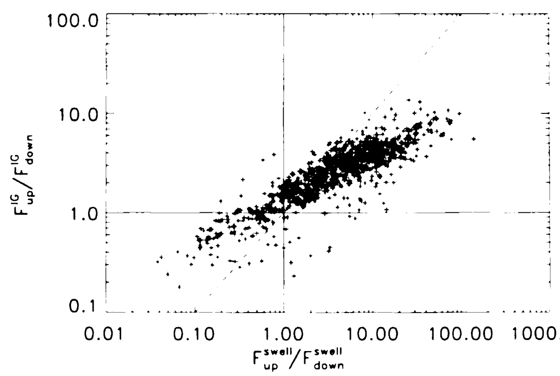

$$\beta(f_1,f_2)=\arctan\left[\frac{-\operatorname{Im}\{B(f_1,f_2)\}}{\operatorname{Re}\{B(f_1,f_2)\}}\right] \tag{A 4}$$

For a three-wave system, Kim & Powers (1979) show that $b^2(f_1,f_2)$ represents the fraction of power at frequency f_1+f_2 owing to quadratic coupling of the three modes ($f_1,f_2,$and f_1+f_2). The biphase is related to the shape (in a statistical sense) of the time series (Masuda & Kuo 1981, Elgar & Guza 1985b, Elgar 1987).

Consider the time series

$$\eta(t)=\cos(f_1t+\theta_1)+\cos(f_2t+\theta_2)+\cos(f_3t+\theta_3) \tag{A5}$$

where $f_3=f_1+f_2$. If the 3 Fourier phases are independent and randomly distributed in $[0,2\pi]$, then the time series will have Gaussian statistics and $b(f_1,f_2)$=0. If $\theta_1$and θ_2 are randomly distributed in $[0,2\pi]$ and $\theta_3=\theta_1+\theta_2+\alpha$, where α is a constant, then although each of the 3 Fourier phases is randomly distributed, the *phase relationship* between the 3 Fourier components is not random. The biphase $\beta(f_1,f_2)=\theta_3-(\theta_1+\theta_2)=\alpha$ and $b(f_1,f_2)=1.0$. Time series given by (A5) have identical power spectra regardless of the presence or absence of phase coupling, but their bispectra differ. Phase coupling occurs in systems where quadratic interactions between the components at frequencies f_1 andf_2 excite motions at their sum frequency f_3.

Figure 16.

Predicted versus observed ratios of upcoast to downcoast alongshore energy fluxes in the infragravity frequency band $F^{IG}_{up}/F^{IG}_{down}$ for 20 cases selected to span a wide range of ratios. (From Herbers et al. 1995a.)

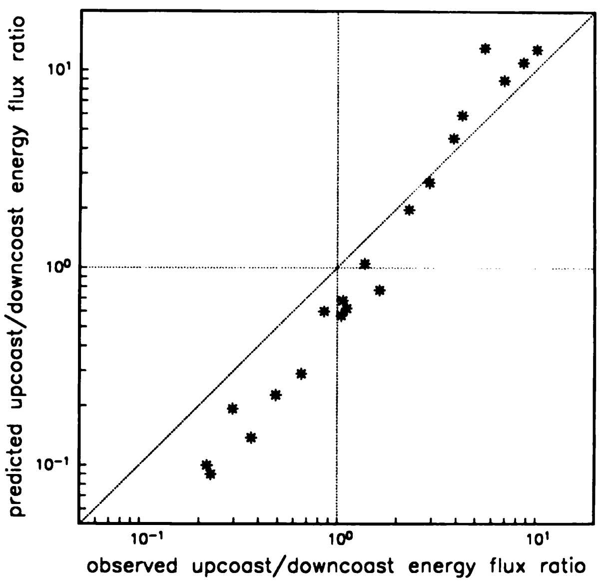

Time series with biphase $\beta(f_1,f_2)=0$ have nonzero skewness (the mean of the cube of the time series, normalized by the variance), and are characterized by wave profiles that have sharp peaks, and broad, flat troughs (an asymmetry with respect to a horizontal axis, figure A1). The contribution of individual frequency triads to the total third moment is given by the bispectrum, similar to the way in which the contribution of individual frequency bands to the variance is given by the power spectrum (Hasselmann et al. 1963). The skewness is the sum of the real parts of the bispectrum normalized by the variance. For a time series with $\beta(f_1,f_2) = -\pi/2$, the real part of the bispectrum and the skewness are zero, but the imaginary part of the bispectrum is nonzero and the time series is asymmetrical with respect to a vertical axis (eg, dashed line in figure A1), and is characterized by fore-aft asymmetric wave forms (eg, the steep front faces and gently sloping rear faces of nearly breaking ocean waves). Asymmetry, a quantity analogous to skewness, is the sum of the imaginary parts of the bispectrum normalized by the variance (Elgar & Guza 1985b, Elgar 1987).

In general, the Fourier components of a nonlinear random process are partially coupled, as opposed to the complete coupling discussed above. If the Fourier component of the sum frequency (f_3) of the example time series in (A5) is given by

$$\cos(f_3 t + \theta_3) = \hat{b}\cos(f_3 t + \theta_{3c}) + \sqrt{1-\hat{b}^2}\ \cos(f_3 t + \theta_{3r}) \quad \text{(A6)}$$

where $\theta_{3c} = \theta_1 + \theta_2 + \alpha$ and θ_{3r} is randomly distributed, then at frequency f_3 the time series contains both a coupled component (with phase θ_{3c}) and an uncoupled component (with phase θ_{3r}). The bicoherence squared $b^2(f_1,f_2) = \hat{b}^2$ is equal to the fraction of the energy at f_3 that is phase coupled to f_1,f_2. The power spectrum is identical to that for the other cases discussed above.

Many observed time series have large background noise levels, but random noise (and nonphase-coupled signals) do not contribute to the bispectrum. However, the detection of weak nonlinear phase coupling in the presence of significant noise is limited by the statistical uncertainty in bispectral estimates obtained from finite length data records. For example, even a truly Gaussian process will yield a nonzero bispectrum estimate if a finite-length time series is examined. Beginning with Brillinger (1965), Rosenblatt & Van Ness (1965), and Brillinger & Rosenblatt (1967a, b) there have been many studies of the statistics of estimates of bispectra. These are not reviewed here. Haubrich (1965), Hinich & Clay (1968), Kim & Powers (1979), Elgar & Sebert (1989), Chandran & Elgar (1991), and others discuss the statistics of estimates of bicoherence and biphase. References to extensions to higher-order (eg, trispectra) spectra can be found in Elgar & Chandran (1993).

Acknowledgements

This research was supported by the Office of Naval Research. V. Chandran, M. Freilich, E. Gallagher, M. Okihiro, J. Oltman-Shay, W. O'Reilly, and B. Raubenheimer have contributed significantly to these studies of nearshore waves. Their contributions are greatly appreciated. The field efforts of D. Alden, W. Boyd, M. Clifton, S. Gavino, P. Harvey, C. Hendricks, P. Jessen, R. Lowe, M. Kirk, K. Millikan, L. Martell, T. Moores, A. Schoenbacher, T. Schwitzer, W. Waldorf, B. Woodward, and C. Worley have been heroic. The Field Research Facility, Coastal Engineering Research Center, Duck, NC contributed valuable data and logistical support. Some of the figures have appeared in the Journal of Fluid Mechanics, the Journal of Geophysical Research, and the Journal of Physical Oceanography.

Biographies

Steve Elgar, a professor at Washington State University, received a Ph.D. from the Scripps Institution of Oceanography in 1985. A long term objective of his research is to understand and model the interactions between complex and changing bathymetry, waves, and circulation observed on natural beaches. An additional interest is the development of analysis of methods to study nonlinear random processes, especially those occuring in nature, such as ocean surface waves.

Thomas H. C. Herbers received his Ph.D. from the Scripps Institution of oceanography in 1990. He is currently an Assistant Professor in the Department of Oceanography of the Naval Postgraduate School. His research interests include ocean surface wave processes on the beach and continental shelf, and data analysis methodology.

R. T. Guza is a professor of Oceanography at Scripps Institution of Oceanography, University of California at San Diego. His ONR-supported research includes the observation and modeling of surface gravity waves and wave-driven flows in shallow water (e.g., on sandy beaches, within harbors and harbor entrance channels, and on the continental shelf). Upcoming work includes collaborative studies of the effect of irregular beach bathymetry on surf zone waves and currents at Duck, N.C.

References

1. Armstrong, J.A., Bloembergen, N., Ducuing, J. and Pershan, P.S., Interactions between light waves in a nonlinear dielectric, *Phys. Rev.* **127**, 1918-1939, 1962.
2. Bailard, J.A. An energetics total load sediment transport model for a plane sloping beach, *J. Geophys. Res.* **86**, 10, 938-10, 954, 1981.
3. Bailard, J.A. and D.L. Inman, An energetics bedload model for a plane sloping beach: local transport. *J. Geophys. Res.* **86**, 2035-2043, 1981.
4. Beach, R. and R. Sternberg, Suspended sediment in the surf zone: response to cross-shore infragravity motion, *Marine Geology* **80**, 61-79, 1988.
5. Berkhoff, J. Computation of combined refraction-diffraction, Proc. 13th Intl. Conference Coastal Engineering, Vancouver, ASCE, 471-490, 1972.
6. Bertherton, F.P., Resonant interactions between waves: the case of discrete oscillations, *J. Fluid Mech.* **20**, 457-480, 1964.
7. Bowen, A. J., Simple models of nearshore sedimentation; beach profiles and longshore bars; in *The Coastline of Canada*, pp. 21-30, Geological Survey of Canada, Ottawa, Ont., 1980.
8. Brillinger, D. An introduction to polyspectra, *Ann. Math. Statist.* **36**, 1351-1374, 1965.
9. Brillinger, D. and M. Rosenblatt, Asymptotic theory of kth-order spectra, in *Advanced Seminar on Spectral Analysis of Time Series* (ed B. Harris) pp: 153-188, Wiley, 1967a
10. Brillinger, D. and M. Rosenblatt, Computation and interpretation of kth-order spectra, in *Advanced Seminar on Spectral Analysis of Time Series* (ed B. Harris) pp: 189-232, Wiley, 1967b.
11. Chandran, V. and S. Elgar, Mean and variance of estimates of the bispectrum of a harmonic random process: an analysis including effects of spectral leakage, *IEEE Signal Processing* **39**, 2640-2651, 1991.
12. Collins, J.I. Prediction of shallow-water spectra, *J. Geophys. Res.* **77**, 2693-2707, 1972.
13. Doering, J.C. and A.J. Bowen, Wave-induced flow and nearshore suspended sediment, Proc. 21st Intl. Conference Coastal Enginering, ASCE, Malaga, 1452-1463, 1988.
14. Elgar, S. Relationships involving third moments and bispectra of a harmonic process, *IEEE Acoustics, Speech, and Signal Processing* **35**, 1725-1726, 1987.
15. Elgar, S. and R.T. Guza, Shoaling gravity waves: comparisons between field observations, linear theory, and a nonlinear model, *J. Fluid Mech.* **158**, 47-70, 1985a.
16. Elgar, S. and R.T. Guza, Observations of bispectra of shoaling surface gravity waves, *J. Fluid Mech.* **161**, 425-448, 1985b.
17. Elgar, S. and G. Sebert, Statistics of bicoherence and biphase, *J. Geophys. Res.* **94**, 10,993-10,998, 1989.
18. Elgar, S. and V. Chandran, Higher-order spectral analysis to detect nonlinear interactions in measured time series and an application to Chua's circuit, *Int. J. Bifurcation and Chaos* **3**, 19-34, 1993.
19. Elgar, S., R.T. Guza, and M.H. Freilich, Eulerian measurements of horizontal accelerations in shoaling gravity waves, *J. Geophys. Res.* **93**, 9261-9269, 1988.
20. Elgar, S., M.H. Freilich, and R.T. Guza, Model-data comparisons of moments of nonbreaking shoaling surface gravity waves, *J. Geophys. Res.* **95**, 16,055-16,063, 1990.
21. Elgar, S., T.H.C. Herbers, V. Chandran, and R.T. Guza, Higher-order spectral analysis of nonlinear ocean surface gravity waves, *J. Geophys. Res.* **100**, 4977-4983, 1995.
22. Freilich, M.H. and R.T. Guza, Nonlinear effects on shoaling surface gravity waves, *Philos. Trans. R. Soc. London* **Ser. A 311**, 1-41, 1984.
23. Guza, R.T., E.B. Thornton, and R.A. Holman, Swash on steep and shallow beaches, Proc. 19th International Coastal Engineering Conference, ASCE, Houston, 708-723, 1984.
24. Hanes, D. and Huntley, D. Continuous measurements of suspended sand concentration in a wave dominated nearshore environment, *Continental Shelf Res.* **6**, 585-596, 1986.
25. Hasselmann, K., On the non-linear energy transfer in a gravity-wave spectrum, I, General theory, *J. Fluid Mech.* **12**, 481-500, 1962.
26. Hasselmann, K., W. Munk, and G. MacDonald, Bispectra of ocean waves, in *Time Series Analysis*, edited by M. Rosenblatt, pp. 125-139, John Wiley, New York, 1963.

27. Haubrich, R.A., Earth noises, 5 to 500 millicycles per second, *J. Phys. Oceanogr.* **70**, 1415-1427, 1965.

28. Herbers, T.H.C. and R.T. Guza, Wind wave nonlinearity observed at the sea floor, Part I: Forced wave energy, *J. Phys. Oceanogr.* **21**, 1740-1761, 1991.

29. Herbers, T.H C. and R.T. Guza, Wind-wave nonlinearity observed at the sea floor, Part II: Wavenumbers and third-order statistics, *J. Phys. Oceanogr.* **22**, 489-504 1992.

30. Herbers, T.H.C. and R.T. Guza, Nonlinear wave interactions and high-frequency sea floor pressure, *J. Geophysical Research.* **99**, 10035-10048, 1994.

31. Herbers, T.H.C., R.L. Lowe, and R.T. Guza, Field observations of orbital velocities and pressure in weakly nonlinear surface gravity waves, *J. Fluid Mech.* **245**, 413-435, 1992.

32. Herbers, T.H.C., S. Elgar, and R.T. Guza, Infragravity-frequency (0.005-0.05 Hz) motions on the shelf, Part I: Forced waves, *J. Phys. Oceanogr.* **24**, 917-927, 1994.

33. Herbers, T.H.C., S. Elgar, and R.T. Guza. Generation and propagation of infragravity waves, *J. Geophys. Res.*, **100**, 24863-24872, 1995a.

34. Herbers, T.H.C., S. Elgar, R.T. Guza, and W.C. O'Reilly Infragravity-frequency (0.005-0.05 Hz) motions on the shelf, Part II: Free waves, *J. Phys. Oceanogr.* **25**, 1063-1079, 1995b.

35. Hibberd, S. and Peregrine, D.H., Surf and runup on a beach: A uniform bore, *J. Fluid Mech.* **95**, 323-345, 1979.

36. Hinich, M.J. and C.S. Clay, The application of the discrete Fourier transform in the estimation of power spectra, coherence, and bispectra of geophysical data, *Reviews of Geophysics* **6**, 347-363, 1968.

37. Holman, R. A., D. Huntley, and A.J. Bowen, Infragravity waves in storm conditions, Proc. 16th Intl. Conference Coastal Engineering, ASCE, Hamburg, 268-284, 1978.

38. Kaihatu, J.M. and J. Kirby, Nonlinear transformation of waves in finite water depth, *Phys. Fluids* **7**, 1903-1914, 1995

39. Kim, Y.C. and E.J. Powers, Digital bispectral analysis and its applications to nonlinear wave interactions, *IEEE Transactions on Plasma Science* **7**, 120-131, 1979.

40. Kirby, J. T. Higher-order approximations in the parabolic equation method for water waves, *J. Phys. Oceanogr.* **91**, 933-952, 1986a.

41. Kirby, J. T. Open boundary condition in the parabolic equation method, *J. Waterway, Port, Coastal, and Ocean Eng.* **112**, 460-465, 1986b.

42. Kirby, J.T. and R.A. Dalrymple, Modeling waves in surf zones and around islands, *J. Waterway, Port, Coastal and Ocean Engineering* **112**, 78-93 1986.

43. Kobayashi, N., G. DeSilva, and K. Watson, Wave transformation and swash oscillations on gentle and steep slopes, *J. Phys. Oceanogr.* **94**, 951-966, 1989.

44. Le Me'haute', B. and J.D. Wang, Wave spectrum changes on sloped beach, ASCE *J. Waterway, Port, Coastal and Ocean Engineering* **108**, 33-47, 1982.

45. List, J. H., A model for the generation of two-dimensional surf beat *J. Geophysical Res.* **97**, 5623-5636, 1992.

46. Longuet-Higgins, M.S., A theory of the origin of microseisms, *Philos. Trans. R. Soc. London* **A243**, 1-35, 1950.

47. Longuet-Higgins, M.S. On the transformation of a continuous spectrum by refraction, *Proc. Camb. Phil. Soc.* **53**, 226-229, 1957.

48. Longuet-Higgins, M.S., and R.W. Stewart, Radiation stresses in water waves: A physical discussion, with applications, *Deep Sea Res.* **11**, 529-562, 1962.

49. Masuda, A. and Y. Kuo, A note on the imaginary part of the bispectrum, *Deep Sea Research* **28**, 213-222, 1981.

50. Munk, W.H. Surf beats, *Eos Trans. AGU* **30**, 849-854, 1949.

51. Nikias, C.L., and M.R. Raghuveer, Bispectrum estimation: A digital signal processing framework, *Proc. IEEE* **75**, 867-891, 1987.

52. Panchang, V., G. Wei, B. Pierce, and M. Briggs, Numerical simulation of irregular wave propagation over a shoal, *J. Waterway, Port, Coastal and Ocean Eng.* **116**, 324-340, 1990.

53. Peregrine, D. H. Long waves on a beach, *J. Fluid Mech.* **27**, 815-827, 1967

54. Phillips, O.M., On the dynamics of unsteady gravity waves of finite amplitude, 1, *J. Fluid Mech.* **9**, 193-217, 1960.

55. Raubenheimer, B., R.T. Guza, S. Elgar, and N. Kobayashi, Swash on a gently sloping beach, *J. Phys. Oceanogr.* **100**, 8751-8760, 1995.

56. Rosenblatt, M. and J. Van Ness, Estimation of the bispectrum, *Ann. Math. Statist.* **36**, 1120-1136, 1965.

57. Radder, A. C. On the parabolic equation method for water-wave propagation, *J. Fluid Mech.* **95**, 159-176, 1979.

58. Tucker, M.J., Surf beats: Sea waves of 1 to 5 minute period, *Proc. Roy. Soc. London* **A202**, 565-573, 1950.

59. Wright, L.D., R.T. Guza, A.D. and Short, Surf zone dynamics on a high energy dissipative beach, *Marine Geology* **45**, 41-62, 1982.

Solitons and the Inverse Scattering Transform: Nonlinear Fourier Analysis for Shallow Water Wave Trains

A. R. Osborne
Istituto di Fisica Generale dell' Università
Via Pietro Giuria 1, Torino 10125, Italy

Fourier analysis is the mathematical technique which allows one to spectrally represent a measured time series as a linear superposition of sine waves. The sine waves may be thought of as a set of *linear basis functions*. However, the fundamental Eulerian equations of motion for surface water wave dynamics are *fully nonlinear* and sine waves are therefore not the ideal set of basis functions. Is there a way to Fourier analyze wave data in order to be completely consistent with the nonlinear Euler equation dynamics? While this problem has yet to be completely resolved, herein I discuss how, *for shallow water wave motion*, linear Fourier analysis may be nonlinearly generalized using the *inverse scattering transform* (IST): In this formulation the basis functions are the well-known classical *cnoidal waves* of Korteweg and deVries[1]. I discuss specifically how a nonlinear wave train may be represented in terms of a *linear superposition of cnoidal waves plus their mutual nonlinear interactions*. This remarkable simplification of the IST formulation has been somewhat of a surprise, particularly because of the complicated nature of periodic inverse scattering theory[2-6]. The strength of Osborne[7] was that such a simplification is possible. The strength of the present paper is that such a simplification has already been made a practical reality. I synthesize several nonlinear wave trains to illustrate the method and then nonlinearly Fourier analyze shallow water wave data from the Adriatic Sea.

Introduction

Important developments in the understanding of nonlinear wave propagation have occurred during the past 30 years. Of particular relevance to the present work is the discovery of a class of physical systems which are called *integrable nonlinear, partial differential wave equations*[8-11]. Equations of this type are said to be exactly solvable in terms of a relatively new method of mathematical physics known as the *inverse scatter-*

ing transform (IST). A number of these integrable equations are applicable to oceanographic situations. These include:

(1) The Korteweg-deVries (KdV) equation, which describes unidirectional shallow water wave propagation.

(2) The Kadomtsev-Petviashvili (KP) equation, which describes two-dimensional shallow water wave propagation.

(3) The nonlinear Schroedinger (NLS) equation, which describes the one-dimensional dynamics of the wave envelope function in both shallow and deep water.

A major focus of the present paper is to give a non-mathematical introduction to certain aspects of inverse scattering theory and to address shallow water wave dynamics from the point of view of the KdV equation. Of particular importance is the discovery, about 20 years ago, of the theory of *periodic and almost periodic solutions of integrable equations* for which the mathematical formulation is called the periodic inverse scattering transform[2-11]. This work revealed remarkable relationships among the Riemann theory of Abelian functions, the spectral theory of Schroedinger operators and algebraic geometry. Exploitation of periodic IST has yielded rather general periodic solutions of large classes of nonlinear wave equations. The technique may be cast in terms of a kind of *nonlinear Fourier analysis*. It is this latter property which is of prime importance for the study of nonlinear, shallow water wave data.

In spite of rather marvellous successes with regard to the theory, it goes without saying that daunting mathematical difficulties have damped practical applications of the results for over 20 years. The study of periodic inverse scattering theory is not normally part of the graduate curricula in most applied mathematics and physics departments, much less in the applied sciences. It therefore should not be surprising that applications of IST to natural wave motions have not been ubiquitous. The present paper is an attempt to provide a simple, physical perspective of some of the major results leading to time series analysis of shallow water waves[7, 12-21]. Not withstanding the level of mathematical difficulty, which is not presented here, the *physical results turn out to be remarkably simple.*

Sine Waves and Linear Fourier Analysis

Linear Fourier analysis allows an arbitrary wave train to be represented as a linear superposition of sine waves of particular amplitudes, frequencies and phases. The sine wave is a travelling wave solution of a *linear wave equation* and the Fourier transform is a spectral solution of the equation (see Fig. 1). An example is the following *linear shallow water equation with dispersion:*

$$\eta_t + c_0 \eta_x + \beta \eta_{xxx} = 0 \qquad (1)$$

Here $\eta(x,t)$ is the free surface elevation as a function of space x and time t. The coefficients $c_0 = \sqrt{gh}$, $\beta = c_0 h^2/6$, are constants depending upon the depth h and gravitational acceleration g. The simplest periodic solution to (1) is a sine wave:

$$\eta(x,t) = \eta_0 \sin(k_0 x - \omega_0 t + \varphi_0) \qquad (2)$$

Figure 1.

An example of linear Fourier analysis. In (a) is the Fourier spectrum, i.e. the amplitudes of the sine waves in the spectrum as a function of wave number. In (b) are the sine waves themselves; their linear superposition gives the synthesized wave train shown at the bottom of the panel.

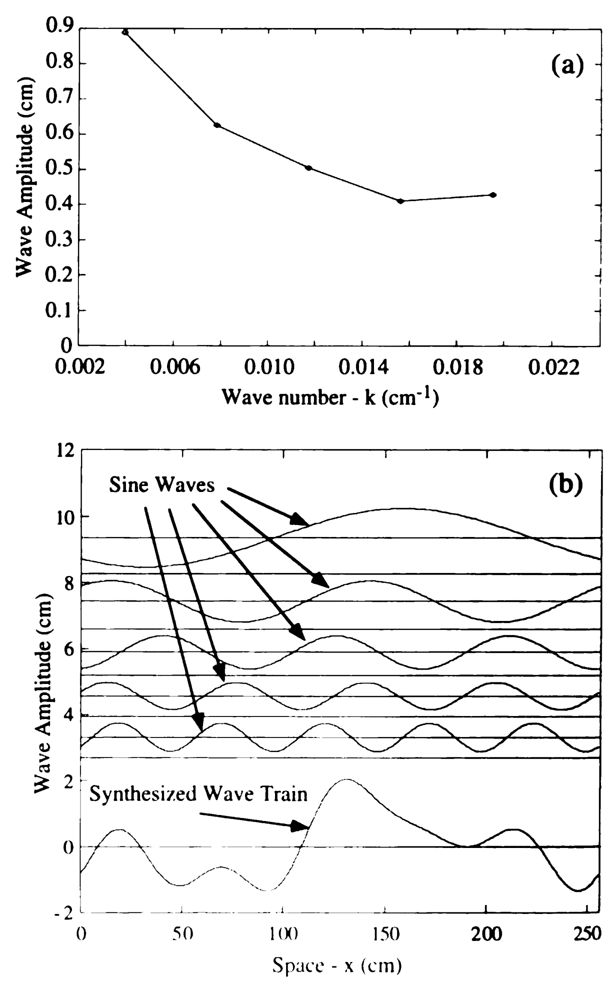

Figure 2.

Examples of cnoidal waves. In (a) is a solitary wave or soliton, in (b) a Stokes wave and in (c) is a sine wave.

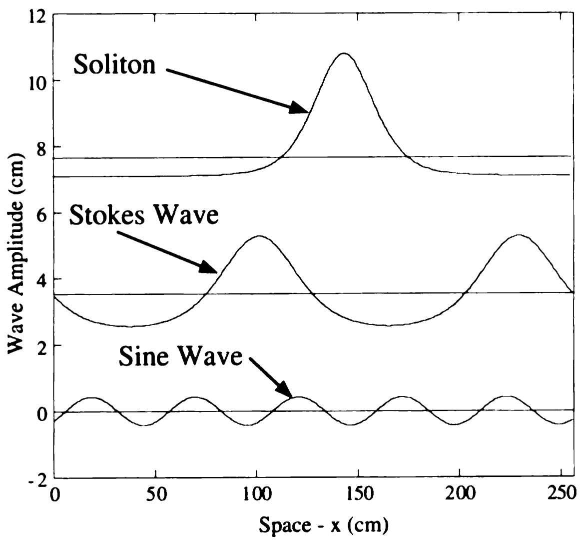

Here η_0 is the wave amplitude, k_0 is the wave number, ω_0 is the frequency and φ_0 is the phase. The Fourier approach allows one to generally solve (1) for periodic boundary conditions, for all space and time, by a linear superposition of the solutions (2):

$$S\eta(x,t) = \sum_{n=1}^{N} \eta_n \sin(k_n x - \omega_n t + \varphi_n) \qquad (3)$$

The sine waves in the Fourier spectrum all have unique amplitudes, wave numbers, frequencies and phases. An important point is that the amplitudes of the sine waves and their phases are *constants of the motion*, provided that the motion is linear. The example of Fig. 1, which has five sine waves, is a solution of equation (1) at time $t = 0$.

Cnoidal Waves and Nonlinear Fourier Analysis

Unfortunately linear Fourier analysis has its limitations, primarily because *shallow water waves are really not linear*. The waves are long with respect to the depth and hence "feel" the presence of the bottom; this effect leads to the presence of nonlinear dynamics. One way that nonlinear effects manifest themselves is by their influence on the shape of the waves. Generally speaking, shallow water waves have crests which are higher and narrower that those for sine waves; by the same token the troughs are less deep and broader relative to sine waves. For waves which are sufficiently high and steep breaking can occur and consequently the free surface, momentarily, may not even be well defined; this is of course the situation in the surf zone. A complete understanding of nonlinear effects in surface water waves has proven to be an extremely difficult mathematical problem; it is enough to recall that the Euler equations for surface wave motion, marvellously complex in their nonlinearity, have remained unsolved for over two centuries.

Since the Euler equations are so difficult to solve one often turns to simpler linear or nonlinear wave equations in order to more easily understand certain physical effects. In shallow water one of the most famous nonlinear equations is that due to Korteweg and deVries[1, 22, 23]:

$$\eta_t + c_0 \eta_x + \alpha\eta\eta_x + \beta\eta_{xxx} = 0 \qquad (4)$$

The constant coefficients here are the same as in equation (1) where $\alpha = 3\, c_0/2h$. Note that equation (4) is the same as (1) except for the addition of the nonlinear term $\alpha\eta\eta_x$. Of course the solution of (1) for periodic boundary conditions is trivial using the linear Fourier transform. The general IST solution to (4) for periodic boundary conditions required an additional 80 years of mathematical progress [8-11]. A simple periodic solution of (4) is the *cnoidal wave*, which is the typical, classical nonlinear wave form often used in shallow water oceanography and offshore engineering [24, 25]:

$$\eta(x,t) = \frac{4k^2}{\lambda} \sum_{n=1}^{\infty} \frac{n(-1)^n q^n}{1-q^{2n}} \cos(nkx) =$$

$$2\eta_0 cn^2 \{(K(m)/\pi)[k(x - Ct);m\} \qquad (5)$$

The modulus m of each elliptic function cn, the nonlinear phase speed C and the nome q are well-known formulas written in terms of the amplitude η_0 [7, 12]; for brevity we do not give them here. The series representation for the cnoidal wave, given in (5), is the *Stokes series* solution to the KdV equation (4). When the modulus $m \to 0$ the cnoidal wave reduces to a sine wave; when $m \to 1$ the cnoidal wave approaches a solitary wave or soliton; intermediate values of the modulus correspond to the Stokes wave (see Fig. 2 for examples). Oceanographic applications of solitary waves were elegantly discussed in one of the early fundamental papers by Munk [26].

Figure 3.

An example of nonlinear Fourier analysis using the inverse scattering transform. There are five cnoidal wave components in the spectrum. In (a) are the amplitudes and the moduli of the spectral components. In (b) are the cnoidal waves and their nonlinear interactions. Linear superposition of the cnoidal waves plus interactions yields the synthesized wave train at the bottom of the panel.

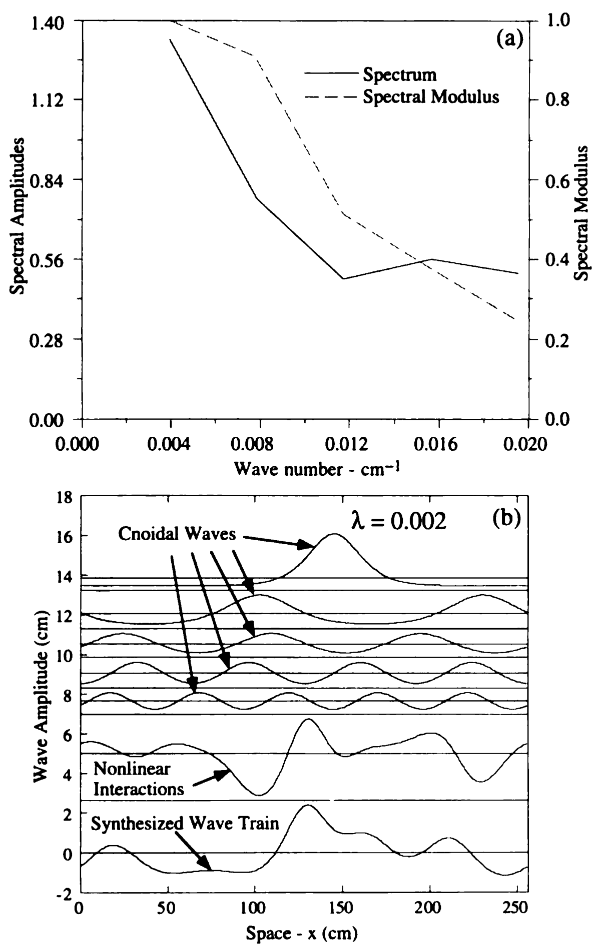

A key question at this point is the following: given that Fourier analysis for linear sine waves exists, does there also exist a *nonlinear Fourier analysis for cnoidal waves*? The major purpose of this paper is to discuss the fact that not only does nonlinear Fourier analysis exist, but it also has been formulated in a physical and mathematical form simple enough that practical oceanographic and engineering applications of the approach are now under way. To show how this formulation arises I give the general solution to the KdV equation (4) in terms of the so-called θ-function representation [2-6]

$$\lambda\eta\,(x,t) = 2\frac{\partial^2}{\partial x^2}\ln\Theta_N\,(\eta_1,\eta_2,\ldots\eta_n), \tag{6a}$$

where the θ-function is given by:

$$\Theta_N\,(\eta_1,\eta_2,\ldots\eta_n) = \tag{6b}$$

$$\sum_{M_1,\ldots M_N=-\infty}^{\infty} \exp\left[\, i\sum_{n=1}^{N} M_n\eta_n + \frac{1}{2}\sum_{m=1}^{N}\sum_{n=1}^{N} M_m B_{mn} M_n \right]$$

Here N is the number of degrees of freedom (or number of cnoidal waves) in a particular solution to the KdV equation. The θ-function phases are exactly the same as in linear Fourier analysis (see equation (3)):

$$\eta_n = k_n x - \omega_n t + \varphi_n$$

where the period matrix $\mathbf{B} = \{B_{mn}\}$, the wave numbers k_n, the frequencies ω_n and the phases φ_n depend upon algebraic geometric loop integrals whose determination is discussed elsewhere [7]. The period matrix **B** is constant and provides the cnoidal wave amplitudes and their nonlinear pair-wise interactions.

Note that the KdV equation (4) is a nonlinear generalization of the linear wave equation (1). Furthermore the cnoidal wave (5) is a nonlinear generalization of the sine wave (2). Finally, the θ-function formulation (6) is a nonlinear generalization of the linear Fourier series (3).

It is straightforward to address the following theorem [7]:

Nonlinear Fourier Analysis Theorem: The θ-function solution (6) to the KdV equation (4) can be written in the following form ($u(x,t) \equiv \lambda\eta(x,t)$, where $\lambda = \alpha/6\beta = 3/2h^3$):

$$u\,(x,t) = 2\frac{\partial^2}{\partial x^2}\ln\Theta_N\,(\vec{\eta}) = \underbrace{u_{cn}\,(\vec{\eta})}_{\text{Linear superposition cnoidal waves}} + \underbrace{u_{int}\,(\vec{\eta})}_{\text{Nonlinear interactions among the cnoidal waves}} \tag{8}$$

The basic result can be stated in words: ***Shallow water wave trains can be represented by a linear superposition of cnoidal waves plus a term which includes the mutual nonlinear interactions among the cnoidal waves.*** When the wave amplitudes are small with respect to the depth, the cnoidal waves reduce to sine waves and the interactions tend to zero; consequently, linear Fourier analysis is recovered! It is in this sense that (8) is a nonlinear generalization of linear Fourier analysis. The cnoidal wave amplitudes are determined by the diagonal elements of the interaction matrix **B** while the interactions are determined by the off-diagonal terms.

It is interesting to contrast the results of this Theorem with linear Fourier analysis. In this latter procedure the sine waves may be viewed as a set of linear basis functions. In the nonlinear problem the basis functions are no longer sine waves but are instead a nonlinear generalization, the cnoidal wave. According to the Theorem the nonlinear theory differs in two ways from ordinary linear Fourier analysis: it generalizes the basis functions from sine waves to cnoidal waves and includes the effect of the nonlinear interactions. This is a marvellously simple result. Fluid dynamicists, oceanographers and engineers are all familiar with the cnoidal wave. Now they can also do Fourier analysis with them thanks to inverse scattering theory and recent related advances [7].

The remainder of this paper is devoted to the use of the above Theorem in both the construction of nonlinear wave trains and in the analysis of shallow-water ocean wave data. In the next Section I discuss a simple five-cnoidal wave solution in some detail; a twelve-cnoidal wave solution is also addressed. Subsequently, I give the IST analysis of measured shallow water waves taken in the Adriatic Sea about 20 km from Venice, Italy.

Figure 4.

An example of two small-amplitude cnoidal waves from Fig. 3 and their interactions.

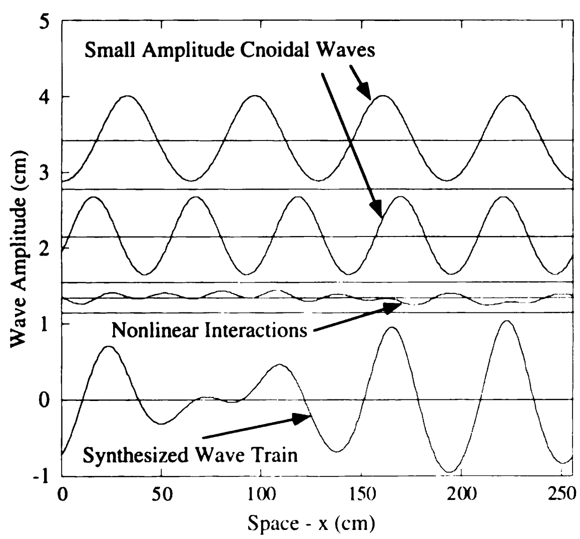

Figure 5.

An example of the interaction between the soliton and a sine wave of Fig.3.

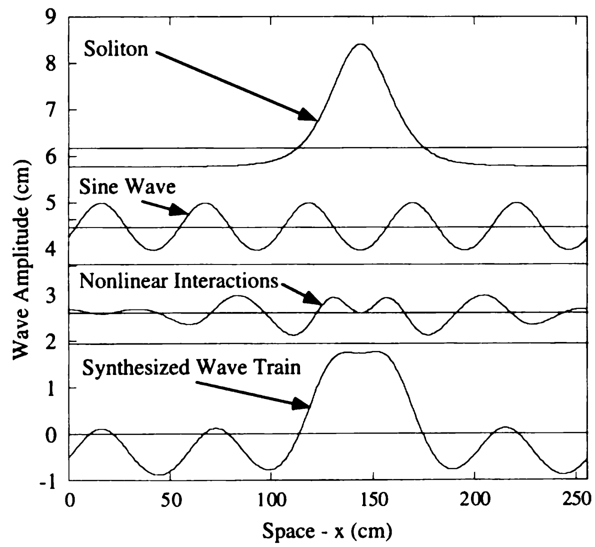

Examples of the Synthesis of Nonlinear Wave Trains using Nonlinear Fourier Analysis

The nonlinear Fourier synthesis of a wave train with 5 cnoidal waves is given in Fig. 3. The cnoidal waves themselves are shown vertically arranged in the upper half of the Figure. The uppermost component has a modulus which is near 1 and is therefore a solitary wave; the remaining components have intermediate values of the modulus and hence are Stokes waves. Below the cnoidal waves in Fig. 3 are shown the nonlinear interactions; the sum of the cnoidal waves plus the nonlinear interactions provides the synthesized wave train itself, as shown in the lower part of the figure. In what sense do the nonlinear interactions participate in the dynamics of the wave train? It can be shown that the interactions have a very simple role: they *phase shift* the cnoidal waves in a collective fashion in order to construct a wave train which is an exact solution to the KdV equation. Thus the interactions shift each cnoidal wave to the right or the left as a function of space and time in order to include the nonlinear coupling among the cnoidal wave spectral components.

There is a simple way to see how the nonlinear phase shifting occurs. Since the interactions are all pair-wise we can look at each pair of cnoidal waves and their nonlinear interactions (see also Boyd [27] and cited references). In Fig. 4 I give the two smallest components of Fig. 3; these waves are so small that they differ very little from ordinary sine waves. However, they do differ slightly from pure sine waves, since the nonlinear interactions, while small, are still significant. The subtle interplay between these two "small-amplitude Stokes waves" is quite nice and interesting. Summation of these waves plus interactions constructs their *contribution to the 5 degree of freedom wave train of Fig. 3.*

Continuing this line of argument, in Fig. 5, I take the first component of Fig. 3 (a soliton) and the last component (practically speaking it is a sine wave) and compute the nonlinear interactions. This constitutes the *interaction of a soliton and a sine wave.* This has been accomplished by extracting the appropriate components from the **B** matrix for the example of Fig. 3 and then reapplying equations (6). Note the symmetric form of the nonlinear interactions about the peak of the soliton. Superposition of the soliton and the sine wave plus the nonlinear interactions yield the synthesized wave train in the bottom of the figure.

Fig. 6 shows the interaction of the first two components of the 5 cnoidal wave example of Fig. 3. Here the components are a soliton and a Stokes wave. The interactions are easily computed and the synthesized wave form is shown at the bottom of the figure. Finally a Stokes wave and a sine wave are studied in Fig. 7. The interactions are computed as before and the resultant synthesized wave train is also given. From these examples we see that the interactions, as computed in pair-wise fashion, are typically stronger between larger cnoidal wave components. The more nonlinear the two cnoidal waves, the greater the pair-wise nonlinear interactions.

Next I give the synthesis of a cnoidal wave train with 12 components. The spectrum is shown in Fig. 8(a) where the cnoidal wave amplitudes (solid line) and the spectral moduli (dotted line) are graphed as a function of wave number. This graph differs *qualitatively* in only one way from that of the linear Fourier transform, e.g. the moduli indicate how nonlinear the individual spectral components are. In this example the first two components are quite nonlinear because their moduli are > 0.97; these components behave like solitons. The remaining components are substantially less nonlinear as the moduli fall below ≈ 0.4; hence these components may be viewed as Stokes waves. The 12 cnoidal waves are shown in Fig. 8(b). The nonlinear interactions have also been computed; note that the largest pulses (effectively largest phase shifts) in the interaction wave train occur for the two peaks in the second cnoidal wave near the top of the figure. The final wave train is synthesized at the bottom of Fig. 8(b).

Figure 6.

An example of the interaction between the soliton and the Stokes wave of Fig. 3.

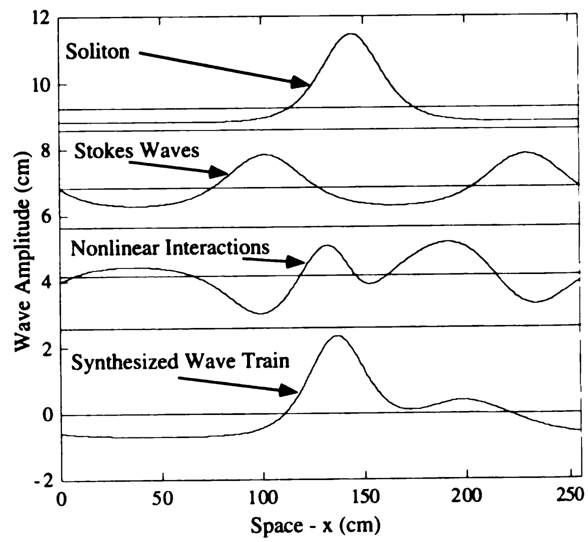

Figure 7.

An example of the interaction between a sine wave and the Stokes wave of Fig. 3.

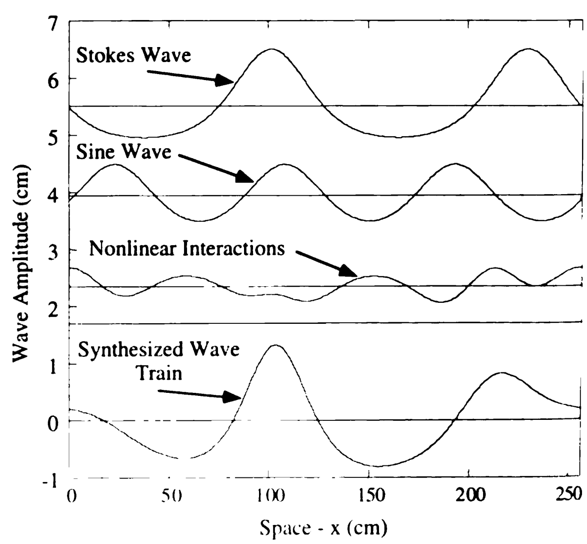

Figure 8.

An example of the nonlinear Fourier synthesis of a wave train with 12 cnoidal waves. In (a) are the spectrum and the moduli of the components as a function of wave number. In (b) are shown the cnoidal waves, the nonlinear interactions and the synthesized wave train.

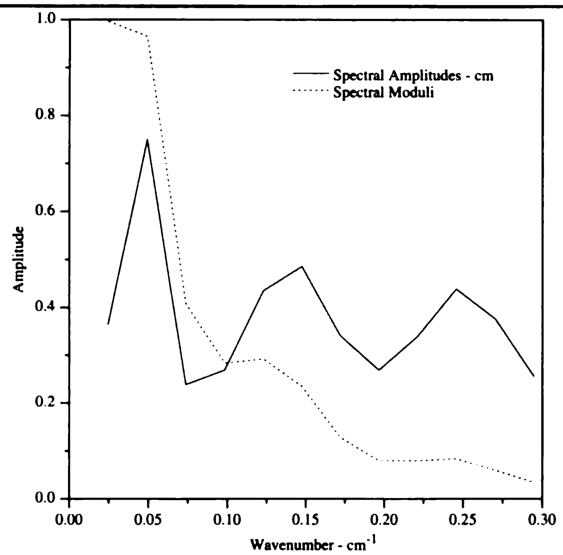

(a)

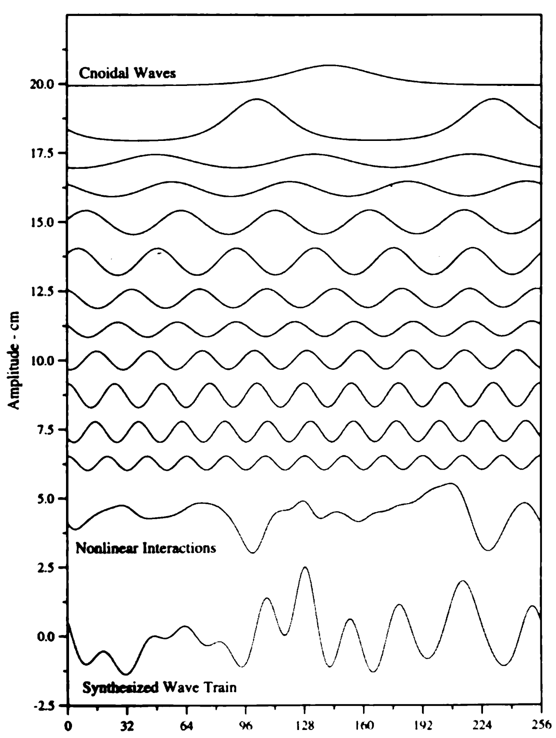

(b)

Figure 9.

A measured surface wave time series from the Adriatic Sea.

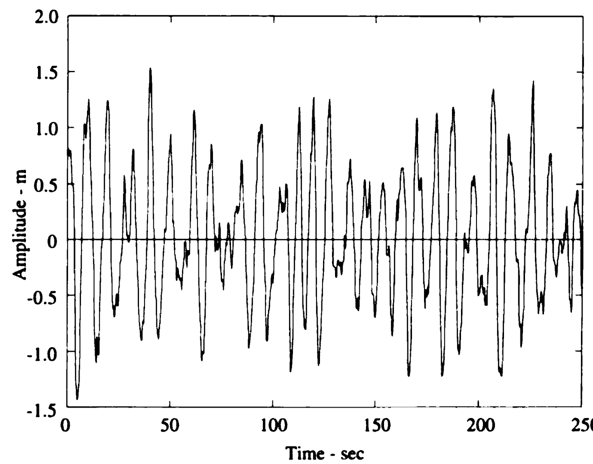

Analysis of Shallow Water Ocean Waves with the Nonlinear Fourier Technique

In the last Section I discussed a number of simple examples of the synthesis of nonlinear wave trains using cnoidal waves. However, a major goal of this research effort is to also analyze real ocean wave data using the IST technique. In Fig. 9 I show a measured wave train from the Adriatic Sea in water of depth 16.5 m [18,19]. The significant wave height is 1.5 m; the largest waves are about 2.5 m in height. The average zero crossing period is 10.1 sec. The inverse scattering transform spectrum is given in Fig. 10. The cnoidal wave spectral amplitudes (solid line) and the moduli (dotted line) are shown. Note the behavior of the modulus, which is large at low frequency and then generally decreases with increasing frequency. The moduli also peak near the peak of the spectrum, rising to about 0.2 at ~ 0.1 Hz. The interpretation of these results is that at low frequency one has several small amplitude solitons in the spectrum, while for the remainder of the spectrum the components can be viewed as Stokes waves of varying degrees of (relatively small) nonlinearity. Fig. 11 gives the first 50 cnoidal waves in the spectrum; truncating the number of cnoidal waves at fifty corresponds to a low pass filtering of the measured wave train in the frequency range 0 to 0.2 Hz. These cnoidal waves have been summed and the result is shown below the cnoidal waves in the figure. The nonlinear interactions have also been computed and these are shown below the summed

Figure 10.

Nonlinear Fourier analysis of the Adriatic Sea time series of Fig. 9. Shown are the cnoidal wave spectrum (solid line) and moduli (dotted line) as a function of frequency.

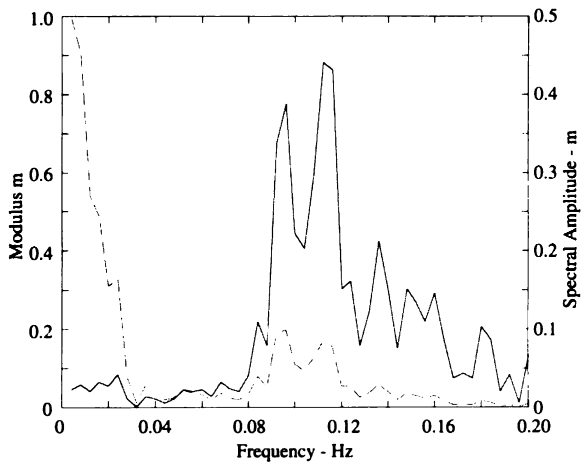

cnoidal waves. Finally the low-pass-filtered time series has been reconstructed at the bottom of the figure.

What have we learned from this exercise? It is clear that the nonlinearity in the measured wave train is not very great. This can be seen in two ways. First, in Fig. 10 one sees that the moduli are small, except for the first two components. A mild enhancement in the modulus occurs near the peak of the spectrum, a result which is to be expected for these larger waves. Second, the train of nonlinear interactions in Fig. 11 is rather small compared to the reconstructed wave train itself. However, even though the nonlinear effects are not very large, they are nevertheless substantial and provide some insight about the behavior of the measured wave train: Note that the sum of the cnoidal waves has larger amplitudes than does the wave train itself. This occurs because the interaction term is *out of phase* with the measured time series. This should not be surprising; we are all familiar with the two soliton interaction in which the solitons *reduce* their amplitudes during a collision. As just seen this effect is also observed in the analysis of this Adriatic Sea wave train. An interesting observation is that because the interactions are relatively small in this case, one might eventually be able to construct a perturbative theory for the nonlinear interactions.

What should happen as the waves propagate into shallower water? As the depth decreases the Ursell number ($\sim 1/h^3$) must rapidly increase. This of course increases the influence of the bottom on the nonlinear dynamics of the wave train. Consequently, on the average the moduli of the cnoidal waves must increase and consequently the nonlinear interactions will also increase substantially. Eventually at some depth all the moduli will have reached 1 and all the cnoidal waves will have become solitons. Thus the term "nonlinear shoaling" takes on new meaning in the context of the inverse scattering transform. The problem of nonlinear shoaling has been previously addressed, not for cnoidal waves, but for the hyperelliptic function representation in references [18, 19].

It goes without saying that IST provides new opportunities for enhancing our knowledge and understanding of nonlinear shallow water waves. Future efforts will address a whole host of interesting nonlinear effects, including resonances and chaos.

Other Applications of Inverse Scattering Theory

Figure 11.

Nonlinear Fourier analysis of the Adriatic Sea time series of Fig. 9. Shown are the first fifty cnoidal waves in the spectrum; this is equivalent to a low pass filter of the measured wave data from 0 to 0.2 Hz. Also shown is the wave train corresponding to the sum of the cnoidal waves, the nonlinear interactions and the reconstructed low-pass-filtered input time series.

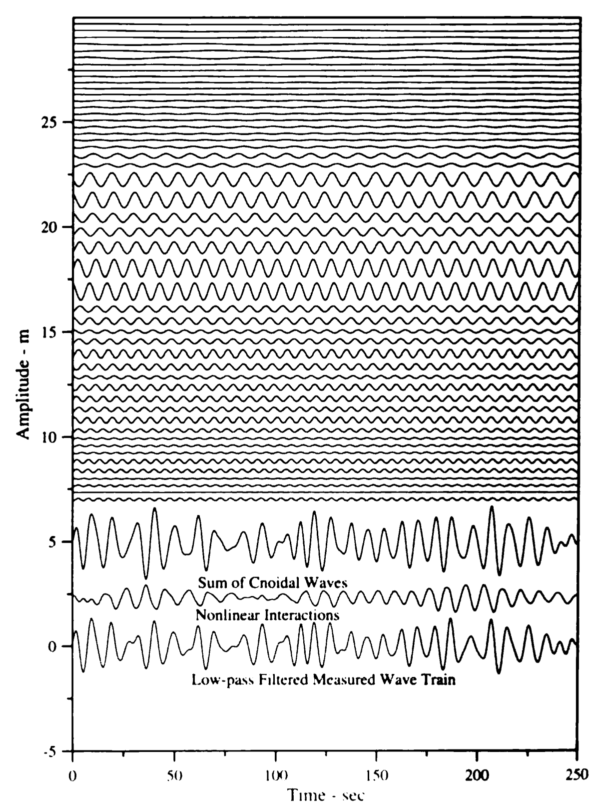

It is worth briefly mentioning that other applications of the inverse scattering technique are readily addressed in the shallow water coastal zone. These include the nonlinear dynamics of internal waves, acoustic wave propagation in the shallow water sound channel and the nonlinear dynamics of surface and subsurface floating vessels. This discussion focuses on present and future directions of research using IST.

The shallow water internal wave field is often describable by the dynamics of the Korteweg-deVries equation [28]. The discovery of large internal solitons by Exxon drilling operations in the Andaman Sea, offshore Thailand, has graphically illustrated the importance of internal waves on operational and design conditions for offshore operations (Osborne, Burch and Scarlet [29]). In this regard a soliton interpretation of the Andaman Sea data, using fundamental results of inverse scattering theory, was made 15 years ago by Osborne and Burch [28]. Subsequently large internal solitons were also found in the Sulu Sea [30] and other continental shelf areas. It thus seems timely that the inverse scattering transform be used to analyzed data of this type in order to enhance our understanding of the solitonic component of the internal wave field.

Acoustic wave propagation on the continental shelf, in regions where KdV dynamics might be applicable, is also an important area of research. It is well-known that internal wave temperature variations in shallow water are often found to obey the Korteweg-deVries equation; because sound speed variations closely follow the temperature variations it is clear that both temperatures and sound speed variations have inverse scattering transform modes. Therefore nonlinear Fourier analysis using the inverse scattering transform can provide additional perspective about sound propagation in these regions.

Finally let me discuss floating body motions. How should the motion of a floating structure be influenced by nonlinear wave motion governed by IST? Can one compute the frequency response function of the vessel under the presence of wave forces due to a nonlinear wave train? The answers to these questions can be addressed in terms of the cnoidal wave modes and their mutual interactions. Let me give a simple illustrative example. Assume that the equation of motion of a floating object in a sea state governed by the KdV equation is given by

$$m\ddot{x} + c\dot{x} + k\,x = F\,(\,t\,)$$

where F(t) is representable in terms of cnoidal waves plus interactions. Then the frequency response function of the floating body is easily determined in terms of the parameters *m, c, k* and *the scattering transform modes*. Therefore floating body motions, as governed by the above equation, may be described in terms of the nonlinear modes of the inverse scatting transform. Inverse scattering transform modes provide a new and unique way to study important problems in ocean engineering. Many more vessel-motion problems are discussed in detail elsewhere [31].

Summary and Discussion

Given the rather simple physical interpretation of nonlinear shallow water wave motion presented herein, why has inverse scattering taken so long to develop into data analysis tools? This is primarily because the development of the approach has required a number of important new steps relating to the practical implementation of nonlinear time series analysis procedures. These steps include:

(1) Closure of all aspects of the mathematical physics.

(2) Development of the requisite numerical methods.

(3) New and insightful experiments.

(4) Development of fast time series analysis algorithms.

(5) Development of physical insight with regard to the predictions of IST.

(6) Development of procedures for the implementation of the algorithms, particularly with regard to nonlinear filtering and data analysis applications.

Many of these topics and others are addressed in some of the cited references.

Further directions in the future application of inverse scattering theory include:

(1) The continued development of faster numerical methods.

(2) Study of resonances in nonlinear shallow water waves.

(3) Study of the onset of chaotic motions.

(4) Extension of the method to two dimensional wave motion and development of the concept of nonlinear directional spectra.

(5) The analysis of large quantities of data, including shallow water surface and internal waves, acoustic waves, floating vessel motions, etc.

(6) Extension of the inverse scattering technique to higher order for the study of larger and shorter waves.

Biography

A. R. Osborne is a professor of physical oceanography and nonlinear physics at the University of Turin, Italy. He has 7 years experience in the field of cosmic ray physics (University of Houston); 13 years experience in the aerospace industry (NASA Manned Spacecraft Center, Houston); 10 years experience in the field of physical oceanography at Exxon production Research Company (Houston) and 16 years in the physics department at the University of Turin. He has consulted for a number of ship and offshore platform certification agencies and for several companies in the offshort industry.

References

1. D. J. Korteweg and G. deVries, Philos. Mag. Ser. **5**(39), 422 (1895).
2. A. R. Its and V. B. Matveev, Func. Anal. and Appl. **9**(1), 65 (1975).
3. B. A. Dubrovin, V. B. Matveev and S. P. Novikov, Russian Math. Surv. **31**, 59 (1976).
4. H. Flaschka and D. W. McLaughlin, Prog. Theoret. Phys. **55**, 438 (1976).
5. E. Date and S. Tanaka, Prog. Theoret. Phys. Supp. **59**, 107 (1976).
6. H. P. McKean and E. Trubowitz, Comm. Pure Appl. Math. **29**, 143 (1976).
7. A. R. Osborne, Phys. Rev. E, **52**(1), 1105 (1995).
8. V. E. Zakharov, S. V. Manakov, S. P. Novikov and M. P. Pitayevsky, *Theory of solitons. The Method of the Inverse Scattering Problem* (Nauka, Moscow (in Russian), 1980).
9. M. J. Ablowitz and H. Segur, *Solitons and the Inverse Scattering Transform* (SIAM, Philadelphia, 1981).
10. R. K. Dodd, J. C. Eilbeck, J. D. Gibbon and H. C. Morris, *Solitons and Nonlinear Wave Equations* (Academic Press, London, 1982).
11. A. C. Newell, *Solitons in Mathematics and Physics* (SIAM, Philadelphia, 1985).
12. A. R. Osborne, Phys. Rev. E **48**(1), 296 (1993).
13. A. R. Osborne, In *Statics and Dynamics of Nonlinear Systems*, ed. G. Benedek, H. Bilz and R. Zeyher (Springer-Verlag, Heidelberg, 1983).
14. A. R. Osborne and L. Bergamasco, Nuovo Cimento B **85**, 2293 (1985).
15. A. R. Osborne and L. Bergamasco, Physica D **18**, 26 (1986).
16. A. R. Osborne, "Nonlinear Fourier analysis," in *Nonlinear Topics in Ocean Physics*, edited by A. R. Osborne (North-Holland, Amsterdam, 1991).
17. A. R. Osborne, J. Comp. Phys. **94**(2), 284 (1991).
18. A. R. Osborne, Proceedings of the Aha Huliko'a Hawaiian Winter Workshop, University of Hawaii Press, ed. by Peter Müller and Diane Henderson (1993).
19. A. R. Osborne, L. Bergmasco, M. Serio and L. Cavaleri, L. Iovenitti, and D. Viegzoli, Nuvo Cemento, 19c(1), 151 (1996).
20. A. R. Osborne and M. Petti, Phys. Rev. E **47**(2), 1035 (1993).
21. A. R. Osborne and M. Petti, Phys. Fluids **6**(5), 1727 (1994).
22. G. B. Whitham, *Linear and Nonlinear waves* (John Wiley, New York , 1974).
23. J. W. Miles, Annual Rev. Fluid Mech. **12**, 11 (1980).
24. R. Weigel, Oceanographical Engineering. Englewood Cliffs, N.J., Prentice-Hall, 1964.
25. T. Sarpkaya and M. Isaacson, Mechanics of Wave Forces on Offshore Structures, Van Nostrand Reinhold, New York (1981).
26. W. H. Munk, N. Y. Acad. Sci. **51**, 376 (1949).
27. J. P. Boyd, Adv. Appl. Mech, Vol. **27**, 1 (1990).
28. A. R. Osborne and T. L. Burch, Science **208**, 451 (1980).
29. A. R. Osborne, T. L. Burch and R. I. Scarlet, J. Pet. Technol. **30**, 1497 (1978).
30. A. K. Liu, J. R. Holbrook and J. R. Apel, J. Phys. Oceanogr. **15**, 1613 (1985).
31. A. R. Osborne, to appear in ASME Transactions (1996).

Effect of Wind and Shear on Surface Waves

Maria Caponi, TRW Space and Technology Division, Redondo Beach, CA
Philip Saffman, California Institute of Technology, Pasadena, CA

Introduction

"However, his (Tevake, a Polynesian navigator) most interesting concept to my mind is that the *shape* of waves in the open sea can sometimes indicate the presence and direction of a current."[1]

Some of the primary sensors for remote investigation of the ocean properties are high frequency radars that respond only to wind sensitive short waves, in the wavelength range of 1 to 10 cm. Hence, the interpretation of radar images of the sea surface requires the understanding of the generation of short waves by wind and their interaction with longer waves and currents. In most oceanic situations, the wind blows over pre-existing waves that are long enough to withstand dissipation. The presence of these waves can significantly affect the interaction properties between the wind and the shorter wind-generated waves. Further, the distribution of the short waves on the phase of the long waves has a strong impact on the interpretation of high frequency radar imaging.

The study of the effect of wind and shear on water waves can be divided into three areas. First, the analysis of the shape of waves of permanent form. Second, the investigation of the stability of a uniform flow with wind and shear to infinitesimal disturbances. Third, the stability of finite amplitude disturbances as well as the stability of the finite amplitude waves of permanent form themselves. Of particular interest here is the effect of the presence of long waves of permanent form on the shape and stability of short waves.

The classical theory of non-linear water waves can be said to have started with the work of Sir Gabriel Stokes in 1847, who calculated the first few terms in the Fourier series expansion of the wave surface for irrotational (i.e. vorticity free) gravity waves of permanent form, and conjectured that there would be a wave of greatest height which would be cusped. In the subsequent nearly 150 years, the field has attracted the attention of leading mathematicians and physicists, including e.g. Einstein[2]. The study of water wave phenomena has stimulated the discovery of novel methods for the exact solution of non-linear partial differential equations (e.g. soliton and inverse scattering theory). The recurrence phenomenon of non-linear dynamical systems, known as the Fermi-Pasta-Ulam phenomenon has been found in water wave experiments and theory (e.g. Yuen and Lake[3]). Theoretical models of non-linear water wave interactions studied by Caponi, Saffman and Yuen[4] display a rich chaotic behavior.

A spectacular experiment by Su et al. [5] exhibited bifurcation of two-dimensional finite amplitude water waves into three dimensional waves of permanent form (figure 1). These waves, by a remarkable coincidence, were being calculated independently at the same time by Meiron, Saffman and Yuen[6] (figure 2). But note that the comparison between the experimental observations and the theory displays an important difference which is not yet adequately resolved; the theoretical waves have fore and aft symmetry, while this is not so for the physical waves. It is an open question whether the symmetry breaking is due to dissipation or nonlinearity.

With the exception of studies directed specifically at the generation of waves by wind, the classical theory generally ignores the dynamics of the air (because the air density is $O(10^{-3})$ smaller than that of the water) and neglects the possibility of shear in the water because the sources of vorticity are weak and the flow is irrotational to a good approximation, at least until wave breaking occurs. However, it is becoming recognized that there may be a number of important phenomena where the dynamical importance of the air and water shear plays a significant role.

"A number of phenomena are still quite unexplained, and are very relevant to engineering problems. For example, it has been known by many generations of sailors that waves produced by wind when it opposes a quite small current are greater than those when the same wind is in the same direction as the current. With 'wind against tide' the sea appears rougher, small ships toss about far more and there is more broken water seen. The effect is much more marked than can be accounted for by the slight increases of relative velocity. Sailors are taciturn folk, and so there are few references to this in the literature, and none at all in scientific work." Francis[7].

In the case of wind generated waves co-existing with a swell, an interesting phenomenon was experimentally demonstrated by Mitsuyasu[8]. The growth of the wind waves can be intensified or attenuated depending whether the swell is propagating against or in the direction of the wind. For the latter case and sufficient swell steepness (nonlinearity) the short wind generated waves and roughness are *swept clean, pushed to the forward face of the steep long wave*; see Mitsuyasu[8], Hsu[9].

The principal theories that explain the transfer of energy from wind to waves have neglected until recently the effect of water shear and long waves. Part of the problem has been the need for analytical theories to use simplifying approximations that limit their range of application. For numerical solutions the difficulty is related to the extensive computations required for an accurate solution of the eigenvalue problems (i.e. wave speed calculations), even for the linear case if a continuous, realistic wind profile is assumed. This limits the possibility of obtaining a complete picture of the dominant effects.

Recently, Caponi et al [10] have analyzed the stability of the air-water interface using idealized wind and water shear profiles that reduce the linear eigenvalue problem to the solution of a quartic equation. The simplification also permits investigation of the effect of finite but small steepness long waves on the overall stability of the short wind generated waves. The simplicity of the model allows a detailed parametric investigation that can be used to focus ideas and compare with detailed numerical investigations (e.g. Morland and Saffman[11], Valenzuela [12]).

The present article describes some of the current research and results associated with the effect of wind, shear and long waves on waves of permanent form and short wave instabilities. The description is concerned with inhomogeneity of velocity; effects of density stratification are not considered, except for the separation into air and water both assumed of constant density. This is not because stratification is unimportant; the contrary is true; but rather because we wish to focus here on effects of shear.

Waves of Permanent Form in the Presence of Shear

There have been many calculations of the shape of finite amplitude, two-dimensional waves of permanent form in the absence of shear and air motion (e.g. Cokelet[13]). When the restoring force is gravity and surface tension is negligible, they are called Stokes waves. Calculations performed during the last 25 years have demonstrated that there is a continuous family of Stokes waves of given wavelength, from infinitesimal waves up to the wave of greatest height $h/\lambda = 0.14107$, whose crests are cusped with interior angle 120°. h is the wave height, defined as the vertical distance between crest and trough, and λ is the wavelength.

The work of Chen and Saffman[14] showed that the family of Stokes waves bifurcates subharmonically into waves of longer wavelength whose crests and troughs are not all of the same height and that the waves are not unique for $h/\lambda > 0.1289$. This is contrary to the long held belief that Stokes waves are unique (i.e. there is only one wave of given height and wavelength apart from a horizontal translation). It was also thought that the Stokes waves had fore and aft symmetry so that from the shape of a steady wave it could not be determined which way it is propagating. Zufiria[15], however, showed that symmetry breaking could occur spontaneously on the bifurcated branches so that waves without fore and aft symmetry exist.

Figure 1.

Bifurcation of two dimensional water waves into three dimensional waves of permanent form. Experimental result. (From Su et al[5]).

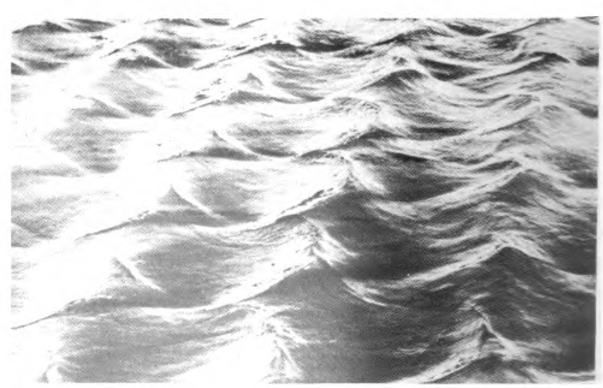

The amount of symmetry breaking is, however, quite small, being about 5% for the steepest wave that can be calculated before the accuracy of the solutions becomes doubtful.

Less work has been done for the case when there is shear or vorticity in the water. For the case of constant vorticity and finite constant depth, for which the undisturbed velocity profile is a linear shear, numerical and analytical methods for small steepness waves were developed by several authors. The results from these studies did not show significant differences from those obtained without shear.

The first work for the case of infinite depth and large steepness waves was carried out by Simmen and Saffman[16]. They used a boundary integral method for a linear shear of infinite extent. This method expresses the solution in terms of an integral of the values of the fluid velocity at the boundary and leads to an integral equation that must be solved numerically. Milinazzo and Saffman[17] used a Fourier series representation of the surface displacement for the case of a linear shear of finite thickness above infinitely deep water, the object being to model a wind drift layer (i.e., a shallow current layer in the ocean ostensibly produced by the drag of the wind). The interesting result was found that shear steepens waves propagating in the direction opposite to the drift current and enhances the tendency for the wave to break. On the other hand the wave is flatter when drift current and propagation speed are in the same direction and the tendency to break is retarded. This effect can be quite strong. The limiting wave height can be reduced to one third of the no shear case when the wind drift velocity is around 50% of the wave speed, and increased by a factor of three when the wave and drift directions are opposite. The results also confirm a heuristic one-dimensional model of breaking by Banner and Phillips[18]. A formulation using a boundary integral method was also carried out for finite depths and large steepness by Teles da Silva and Peregrine[19]. The results obtained from this study are similar to those obtained from the infinite depth case.

The families of waves of permanent form with shear also exhibit subharmonic bifurcation into longer waves with more structure. Indeed, because the shear makes the undisturbed flow non-symmetric, it could be anticipated that the breaking of fore and aft symmetry occurs in the main branch family (i.e. waves that are analytic continuations with respect to shear of the Stokes waves). Surprisingly, this is not the case and the main branch family has fore and aft symmetry for all heights up to the maximum. Symmetry breaking does exist along the subharmonic bifurcation branches and is enhanced by shear (Baumstein[20]). Figure 3 shows a main branch wave and a subharmonic symmetry breaking member of the bifurcated branch.

To date, the calculations for the shapes of waves of permanent form are restricted to two-dimensional disturbances of piecewise linear, undisturbed velocity profiles (sometimes called stick profiles) for mathematical reasons. In this case, vorticity is a conserved quantity, which does not need to be solved for, and the disturbance is irrotational. The mathematical techniques of potential theory can then be applied and the problem formulated using complex variable theory. In particular, boundary integral methods can be employed, that are free of the convergence difficulties that can arise with the use of truncated Fourier expansions. The choice of numerical method plays an important role in this type of calculation. However, it is not essential to restrict attention to stick profiles and current work by us is studying the form of permanent waves on continuous profiles of velocity or vorticity. The extension to three-dimensional waves is a very difficult problem which appears to be beyond present analytical and numerical capabilities.

Effect of wind and water shear on wave instabilities

There are two aspects of the way in which wind and shear, or vorticity in the air and water, affect the instabilities of surface waves at an air-water interface.

First, there is the question of the instability of existing waves, generated mechanically for example, or by earlier winds. In this situation, the dynamics of the air is unimportant and the hydrodynamics of the water motion is the dominant factor. The second aspect is concerned with wave generation by wind or current. In particular, we can consider the generation of waves as a problem of the linear hydrodynamic instability of a laminar flow.

Instabilities of existing waves

The instabilities of wave trains can be categorized, for convenience, into three types, as follows.

Figure 2.

Bifurcation of two dimensional water waves into three dimensional waves of permanent form. Theoretical result. (From Meiron, Saffman and Yuen[6])

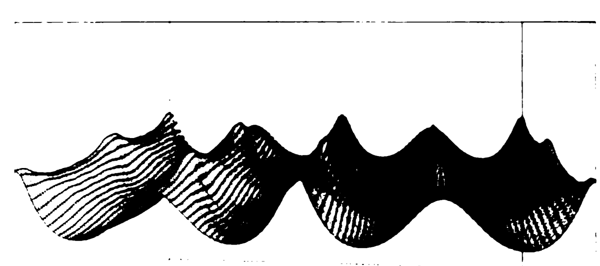

(i) Resonant interactions, Phillips[21]: This describes the transfer of energy between wave trains of vector wavenumbers k_i and frequencies ω_i when $\sum k_i = 0$ and $\sum \omega_i = 0$.

(ii) Two- and three-dimensional long wave envelope modulations or side band instabilities: These go generally under the name of the Benjamin and Feir[22] instability. Instabilities of this kind were also described by Lighthill[23] (who used Whitham's variational principle), Zakharov[24, 25] and others.

(iii) Two- and three-dimensional, sub- and super-harmonic instabilities of finite amplitude waves of permanent form: The two-dimensional case was studied by Longuet-Higgins[26]. Saffman[27] and MacKay and Saffman[28] applied a Hamiltonian formulation to explain qualitatively some of the results such as the change of stability when the wave energy as a function of wave height is stationary or modes collide. This type of formulation makes it possible to follow a change in the eigenvalues (i.e. growth rate of the disturbance) as a control parameter such as the wave height is varied. The three-dimensional case was studied by McLean, Ma, Martin, Saffman and Yuen[29], see also McLean[30]; we shall refer to this as the MMMSY instability.

Figure 3.

Waves of permanent form with shear. a) Main branch wave. b) Subharmonic bifurcation branch illustrates symmetry breaking due to shear.

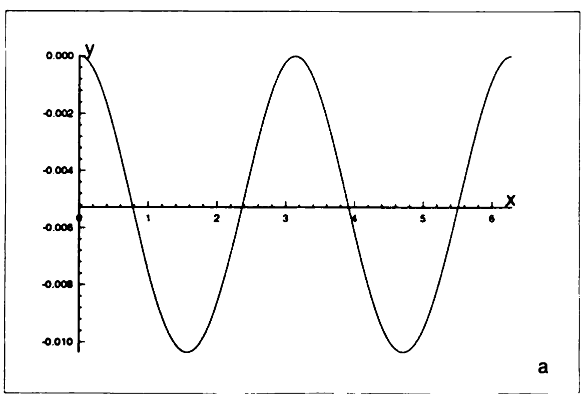

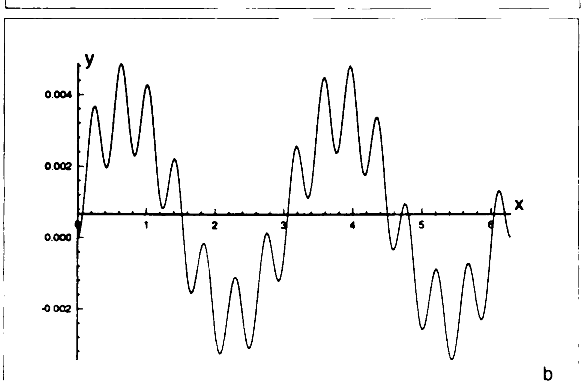

Although the phenomena in (ii) and (iii) can be regarded as particular cases of (i), it is useful to categorize them separately since for those cases the small disturbances grow at slow but exponential rates rather than the linear rate usually associated with the resonances of (i).

The resonances and envelope modulations are basically slowly varying, weakly nonlinear phenomena, and the modifications due to shear will arise primarily through changes in the linear dispersion relations (i.e. the relations between wave frequency and wavelength) and the speed of weakly nonlinear, uniform wave trains. For example, Li, Hui and Donelan[31] have calculated the effect of constant water shear on the side-band instability for the case of infinite depth, and found that small shear tends to enhance instability whereas large shear tends to suppress it.

The effect of shear on the MMMSY wave instabilities is a more difficult problem as potential theory cannot be used to relate perturbations of the flow to perturbations of the surface. Also, we cannot use the mathematical simplifications due to existence of a scalar stream-function as it does not exist for three-dimensional long wave disturbances. However, Benney and Chow[32] have used perturbation methods for weakly nonlinear waves and found that weak shear generates relatively strong three-dimensional long wave instabilities. The properties of the instability are significantly different from those of the Benjamin and Feir type. For finite amplitude waves and zero surface tension, Okamura and Oikawa[33] have calculated the instability of two dimensional waves of permanent form to three-dimensional disturbances. They recover the finite depth MMMSY results (McLean[34]) as the shear tends to zero. They also see the Benney-Chow long oblique waves, which are absent when there is no shear.

Wave generation by wind or current

Three basic theories have been used until recently to describe the generation of waves by wind or water shear.

(i) Kelvin-Helmholtz instability: This is the classic instability of a vortex sheet, modified by a density difference between the fluids on the two sides of the sheet.

(ii) Miles[35] instability: This is the transfer of energy from a shear flow in the air over water initially at rest into waves whose phase speed lies between the minimum and maximum of the wind velocity. It has been investigated by Morland and Saffman[11] as an inviscid hydrodynamic instability of a smooth profile. This formulation leads to an eigenvalue problem for the wave speed and growth rate involving a solution of the Rayleigh equation. Modern computers and methods which locate the eigenvalues in the complex plane make the problem easy to solve numerically and render unnecessary the hard analysis of the critical layer, where the fluid velocity equals the wavespeed. This is also the case when an exponential profile is chosen so that the Rayleigh equation has exact solutions in closed form in terms of hypergeometric functions.

(iii) Drift layer instability: This is the hydrodynamic instability of a current with shear in the water, which could be produced, for example, by the drag of the air over the water or mechanically by running a stream over the surface, as for example in an estuary. It was investigated by Esch[36] for gravity waves on piecewise linear profiles, by Stern and Adam[37] for capillary-gravity waves on piecewise linear profiles and by Morland, Saffman and Yuen[38] for capillary-gravity waves on smooth profiles. These treatments are all inviscid and the direct effect of viscosity on the wave evolution is neglected. Viscosity may, of course, play an important role in the generation of the shear profiles, but this is assumed to be on a much longer time scale than that of the instability. Viscosity is sometimes employed to circumvent analytical difficulties associated with a critical layer; this introduces the Orr-Sommerfeld equation (e.g. Valenzuela[12] and subsequent studies of coupled air-water shear flows). But a consistent purely inviscid treatment is possible and the critical layer need not be considered, as mentioned above. It is interesting that a necessary condition for the existence of the drift layer instability is that the drift layer surface velocity U_d, say, is larger than $c_m = (4gT)^{1/4}$, the minimum phase speed of capillary-gravity waves (g is the acceleration due to gravity and T is the surface tension). It is also found that co-flowing waves are stable, and that the unstable waves tend to be moving very slowly.

The mechanism for the generation of waves by drift layer instability is qualitatively attractive. It also provides a delay mechanism for the wave generation after a wind starts blowing, because it is found that the instability mechanism will not work until the layer thickness Δ reaches a critical value as shown by Morland, Saffman and Yuen[38] and Caponi et al[39]. But quantitative predictions are very poor. The necessary condition $U_d > c_m$ is not satisfied by the wind drift layer, and the predicted phase speeds are of order $\frac{1}{2}c_m$ which is much too fast to be consistent with observation. On the other hand, the theory may be applicable to tidal flow in the presence of wind. An onshore wind, for example, would tend to amplify counter flowing waves on an ebbing tide which would be unstable and produce choppiness, whereas unstable waves would not be supported with an onshore wind and a rising tide and the surface would remain relatively smooth.

A further mechanism (Phillips[40]), in which waves are generated by random pressure fluctuations due to a turbulent wind will not be considerer here. For this case, the main effect of shear is the small modification of the dispersion relation.

Recently a model has been developed that encompasses the three main basic theories and because of its simplicity allows a detailed parametric investigation of the characteristics of wind generated waves, adding new insights of benefit to remote sensing. This model is described in the next section.

A simple model of wind shear interaction

The difficulty of the problem is increased when both wind and water shear are included in the analysis of the generation of water waves. A model by Caponi, Caponi, Saffman and Yuen[10], hereafter called the CCSY model, makes use of a piecewise linear profile to simplify the problem and has led to the prediction of interesting new phenomena in the behavior of wind generated water waves. The advantage of using such a profile is that the system dispersion relation becomes a quartic equation in the complex frequency and the parametric dependence of the solutions can be easily examined. Although models that make use of smooth profiles can result in more accurate growth rates they require at best (e.g. for the case of exponential profiles) the solution of dispersion relations consisting of transcendental equations involving hypergeometric functions. An overall understanding of the effects involved becomes more limited the more complex the dispersion equation. This is due to the extensive computations necessary to obtain a detailed dependence of the wave characteristics (e.g. phase velocity, growth rate, wavelength) on the various parameters of interest (e.g. shear layer thickness, wind velocity, etc.)

The idealized undisturbed horizontal velocity profile used in the CCSY model is (see figure 4)

$$U(y) = \begin{cases} 0 & \text{if } y < -D_{wi} \\ U_w + Uwy/D_w & \text{if } -D_w < y < 0 \\ U_w + Uay/D_a & \text{if } 0 < y < D_a \\ U_w + U_a & \text{if } y > D_a. \end{cases}$$

This represents a double shear layer in the air and in the water. An infinitesimal wave-like disturbance with frequency ω and wave number $k = 2\pi/\lambda$ is imposed, and an inviscid fluid assumed. Linearization about a flat surface reduces the momentum and continuity equations to a single equation for the y-dependence of the vertical velocity $v(y)$. In each of the four regions, the solution takes the form $v_n(y) = A_n e^{ky} + B_n e^{-ky}$, where $n = 1,2,3,4$ according to the region. The boundary conditions: continuity of the vertical displacement and pressure across all boundaries, and vanishing velocity at great height and depth are used afterwards to obtain a dispersion relation between the frequency ω and wave number k. The relation can be expressed as a quartic equation for the ratio of the complex wave frequency (real frequency + i growth rate) to the gravity–capillary waves frequency as a function of known constants (gravitational acceleration, surface tension, density of air and water), the relative water to air velocity and dimensionless parameters kD_a, kD_w and the ratio of the wind speed (U_a) to the phase velocity of the gravity–capillary waves (c_0). The assumption of continuity of tangential stress and a fixed percentage for the relative water to air velocity, $U_r = U_w/U_a$, is used to reduce the results to a single stability diagram in kD_a vs U_a/c_0 space.

The results are illustrated in figures 5, 6 and 7. These figures show contours of constant γ/ω_0, the ratio of the growth rate to the intrinsic frequency of the gravity–capillary waves at intervals of 0.1. Figure 5 corresponds to a water–air ratio of 0 04, consistent with the common estimate derived from observations of drift velocities. Figures 6 and 7 illustrate the variations in the stability diagram due to either larger or negligible U_r. In the figures the instability region (the shaded area) is defined by $\gamma/\omega_0 \neq 0$.

The overall stability is strongly dependent on water drift and wind velocity. For example, in the absence of water drift (figure 7), the instability region generally comprises two regions arising from two separate pairs of complex roots of the quartic equation. Region A is consistent with the critical layer analysis of Miles [35]. It occurs for winds below 6 *m/s*, the phase velocity of the unstable waves is approximately the phase velocity of the gravity capillary waves, the growth rate increases with U_a/c_0 and the instability region narrows and asymptotes to U_a/c_0 when $kD_a >> l$. Region B represents an extension of the classical Kelvin–Helmholtz instability mechanism to finite drift layers. It occurs for winds above 6 *m/s*, the wave's phase velocity in this region is much smaller than c_0 and the growth rate much larger than in Region A with a parameter dependence in agreement with Kelvin–Helmholtz instability.

In the presence of water drift (see figures 5 and 6) an intermediate region develops for winds between approximately 4 *m/s* and 6 *m/s*, where the growth rate decreases as U_r increases. Of particular interest is the existence of a range of

Figure 4.

Idealized wind profile and geometry for CCSY model.

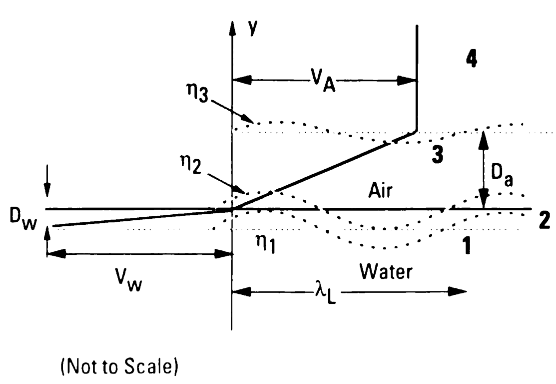

Figure 5.

Unstable region for water to air velocity ratio of .04 (shaded area). Solid lines are contours of constant ratio of growth rate to intrinsic frequency of the gravity-capillary waves at intervals of .1.

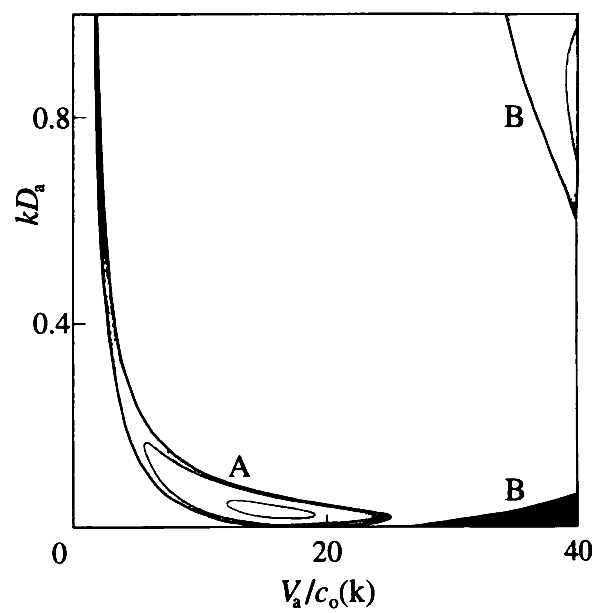

stable wavenumbers for $U_r > 0.03$ and the deduction that different wave components of a disturbance behave differently under a given wind in the presence of water shear. This prediction can be critically tested by experiment. If validated, this prediction may suggest a new design for radar scatterometers with simultaneous multifrequency radars which can more accurately deduce the wind speed by taking advantage of the difference in behavior and history of backscatter returns from different frequency channels. The existence of regions where short waves surrounding the wave of minimum speed do not grow also indicates a potential effect of the presence of long waves on the short waves (cf. next section).

A study similar to the CCSY analysis, that makes use of n multilayers and includes nonlinear effects, has been carried out by Gertsenshtein, Romashova and Chernyavskii[41]. The results presented in that paper do not agree with those of CCSY and unfortunately the article does not present sufficient detail to understand the source of disagreement.

A study of the instability for continuous profiles has been carried out by Hill[42]. Apart from a change of scale of the growth rates, the results are qualitatively similar to those of CCSY. In this case the source of difference in growth rate is the infinite curvature assumed in the piece-wise linear profiles at a change of slope.

Non linear interactions

An interesting and important question is the alteration of the growth rate of the linear instabilities caused by wind and water shear when a long wave of permanent form is present. In the absence of wind and for stable long waves this is the modification of the MMMSY problem by non-uniform water shear. For capillary gravity waves, it is possible that there might be enhanced instability because water shear causes extra corrugation of the interfaces (Milinazzo and Saffman[17]). Preliminary calculations indicate that the swell can reduce the growth rate of the MMMSY instability, but the effect is, however, not large.

For the case of wind but no water shear, an extension of the CCSY analysis has been carried out to study the effect of pre-existing waves of wavelength λ_L on the stability of shorter wind generated waves of wavelength $\lambda_s = \lambda_L/2$ (Caponi [43]). The analysis assumes infinitesimal wave perturbations riding on longer wave disturbances of finite amplitude a. The displacements at each interface i (see figure 4) are then assumed of the form: $\eta_i = \eta_{iL} + \eta_{is}$ with $\eta_{iL} > \eta_{is}$, where $\eta_{iL} = a \cos(k_L x)$.

The dynamic and kinematic boundary conditions are expanded about the long wave displacement and only terms of order $k_L a$ are kept. A system of equations is obtained that is linear in the perturbations and has coefficients of periodicity $2\pi/k_L$. These equations can be solved by expanding the perturbations in Fourier series of the form: $\eta_{is} = \sum \eta_{n,i} e^{ink_L x}$ with $\eta_{n+1,i} << \eta_{n,i}$. These assumptions reduce the problem of finding the system dispersion relation to that of finding the zeroes of the determinant of a matrix M, whose coefficients are functions of the wave frequency, growth, wavelength and the system parameters. Unfortunately, for a system consisting of 4 interfaces and keeping terms of order n in the expansion, M is of order $(9\,n)^2$. The sparcity of the matrix determinant results in a dispersion equation of order $4n$ in the complex frequency, which defeats the purpose of a simple model for large n.

For a system with only wind shear and n=2, M is of order 12 x 12, which is analytically manageable although algebraically cumbersome. The problem can be reduced to a dispersion equation of order 6 in the complex frequency that has an interesting analytical form. Basically it corresponds to the linear (either CCSY or gravity capillary) dispersion relation of the waves of wavelength k_L coupled to the linear (CCSY) dispersion relation of the waves of wavelength $2k_L = k_s$ by a term proportional to the longer wave slope squared. The coupling term is a function of the system parameters and the wave

Figure 6.

Unstable region for water to air velocity ratio of .057 (shaded area). Solid lines are contours of constant ratio of growth rate to intrinsic frequency of the gravity-capillary waves at intervals of .1.

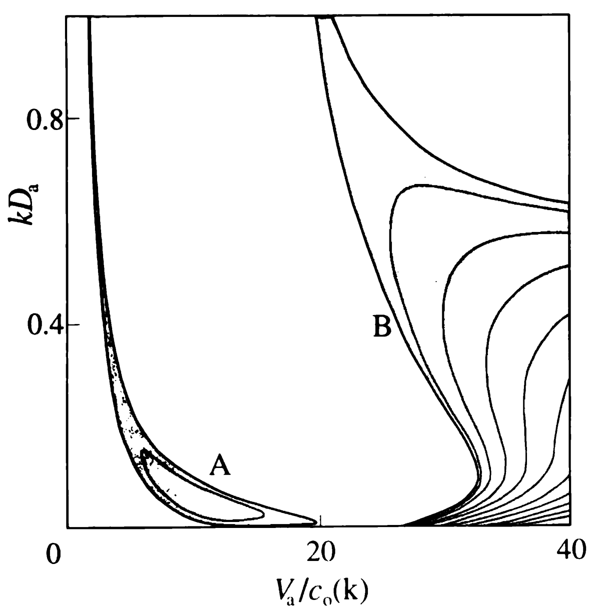

Figure 7.

Unstable region for water to air velocity ratio of 0.0 (shaded area). Solid lines are contours of constant ratio of growth rate to intrinsic frequency of the gravity-capillary waves at intervals of .1.

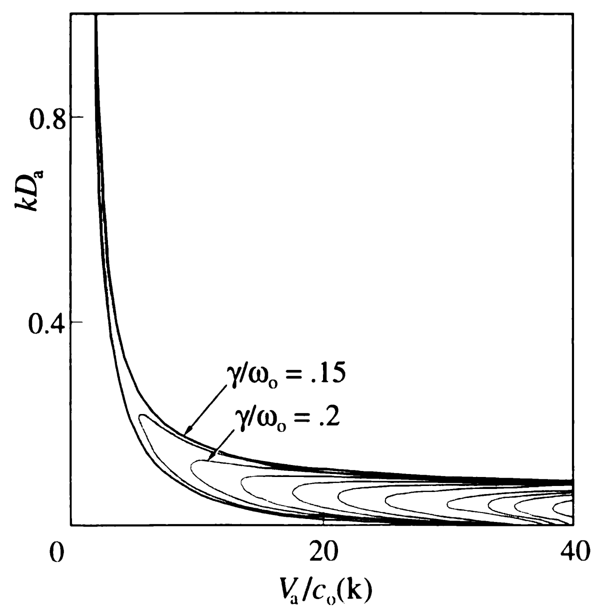

Figure 8.

Unstable region for a long wave of ka = .02 moving in the same direction as the wind, water to air velocity ratio of 0.0 (shaded area). Solid lines are contours of constant ratio of growth rate to intrinsic frequency of the gravity-capillary waves at intervals of .1. Dashed lines enclose unstable region in the absence of the long wave (see figure 7).

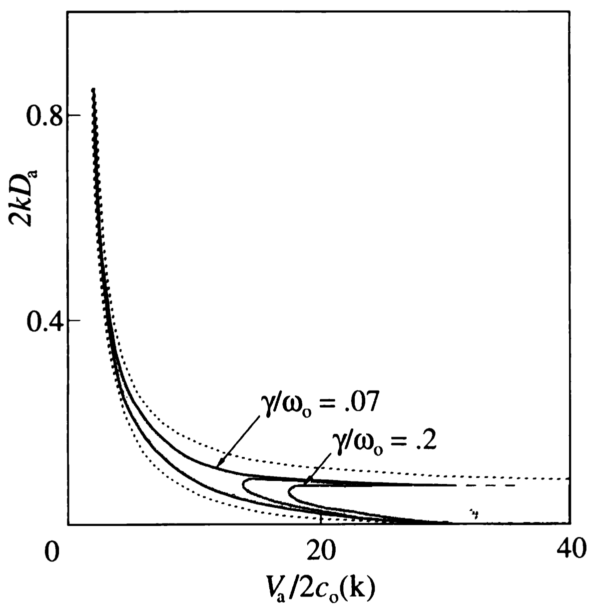

Figure 9.

Unstable region for a long wave of ka = .02 moving in the opposite direction to the wind, water to air velocity ratio of 0.0 (shaded area). Solid lines are contours of constant ratio of growth rate to intrinsic frequency of the gravity-capillary waves at intervals of .1. Dashed lines enclose unstable region in the absence of the long wave (see figure 7).

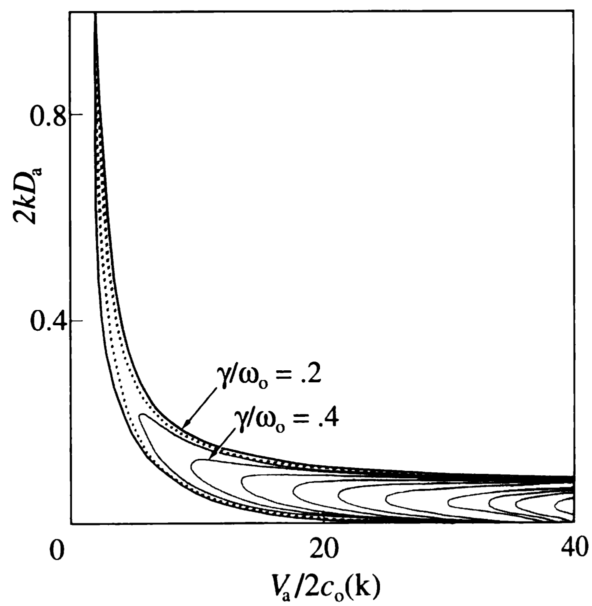

characteristics, its sign determines if the presence of the long wave enhances or reduces the growth of the shorter wave. The stability diagrams of figures 8 and 9 illustrate this effect. In these figures, the dashed lines enclose the unstable region in the absence of long waves, see figure 7.

Figure 8 corresponds to a long wave with a slope of 0.02 moving in the same direction as the wind. The effect is *stabilizing*, the instability region becomes smaller and the value of the growth rate inside the region is reduced. The effect is stronger the larger the value of the longer wave slope, the unstable region becomes negligible as $k_L a \rightarrow 0.04$. Figure 9 illustrates the case of the effect of a long wave moving *opposite* the direction of the wind. In this case the growth rate and the growth region are *enhanced*. These results are very important because they offer a potential explanation for the *sweep up* mechanism (Yuen [44]). Further, they are in agreement with recent experimental measurements by Mitsuyasu[8] and Hsu[9]. For n=2, the Caponi analysis is currently being further extended to include water shear in order to analyze the effect of long waves on the predicted stable region.

For the case of arbitrary n it is possible to formally analyze the system to obtain the general form of the dispersion relation (Caponi [45]). It was found that the general dispersion relation of the system could be written as a coupling between the linear (CCSY) dispersion relations for each harmonic. The coupling term in this case can be written as a sum of n terms each one proportional to the slope of the longer wave to the j power with j running from 2 to n. This result illustrates the coupling of higher harmonics with the fundamental long wave as well as the dependence on the long wave slope. The analysis, however is only formal and can not be used to obtain a quantitative result.

In order to investigate the stability of short waves with $\lambda_s << \lambda_L$ it is necessary to use a different approach. Troitskaya[46] utilized a multiple spatial scale expansion to study the case of wind but no water shear. Her results seem to indicate that the growth rates associated with the Miles instabilities can be significantly reduced in the presence of the longer waves, again in agreement with observation. Caponi and Saffman [47] are currently investigating an expansion that makes use of the assumption that the effect of the very long waves on the unstable short waves occurs on a time scale that is slow compared to the short wave inverse frequency. The approach includes the effect of nonlinear wave-wave interaction and modulational instability promising to encompass previous nonlinear treatments.

Acknowledgements

The authors wish to acknowledge the support of this work by the Office of Naval Research under the Nonlinear Ocean Waves Initiative.

Biographies

Maria Z. Caponi is a Senior Staff Scientist at the Department of Ocean Technology of the Space and Technology Division at TRW. She received her Ph.D. in Physics and Astronomy from the University of Maryland and a subsequent fellowship from the Center for Theoretical Physics to work in nonlinear plasma physics problems. For the last five years she has been doing research in the area of nonlinear ocean wave interactions and their effect on remote sensing of the ocean.

Philip Saffman is the Theodore von Karman professor of applied mathematics and aeronautics at the California Institute of Technology. He was educated at Cambridge, where he was a student of G.K. Batchelor and Sir Geoffrey Taylor, and was elcted a prize fellow of Trinity College. His interests lie in the field of analytical and computational fluid mechanics. He is a fellow of the Royal Society of London and the American Academy of Arts and Sciences.

References

1. D. Lewis. We, the Navigators. The Ancient Art of Landfinding in the Pacific. U. Hawaii Press, Honolulu. (1975)
2. A. Einstein, Die Naturwissenschaften 34, 510 (1916)
3. H.C. Yuen and B.M. Lake, Phys. Fluids 18, 956 (1974)
4. E.A.Caponi, P.G. Saffman and H.C. Yuen, Phys. Fluids 25, 2159 (1982)
5. M-Y Su, M. Bergin, P. Marler and R. Myrick, J. Fluid Mech. 124, 45 (1982)
6. D.I. Meiron, P.G. Saffman and H.C. Yuen, J. Fluid Mech. 124, 109 (1982)
7. J.R.D. Francis. Of shoes ... and ships... and sealing wax... Inaugural Lecture, Imperial College, London. March 1967.
8. H. Mitsuyasu, Wave breaking in the presence of wind drift and opposed swell, in *Breaking Waves*, p. 147, M. L. Banner and R. H. J. Grimshaw, Eds., IUTAM Symposium Sydney/Australia, 1991, Springer-Verlag 1992. See also references therein.
9. C. T. Hsu, Interaction of turbulent winds with small and large amplitude water waves, Internal TRW report, TURBWIND1988, 1988 and personal communication.
10. E.A. Caponi, M.Z. Caponi, P. G. Saffman and H.C. Yuen, Proc. Roy. Soc. A438, 95 (1992).
11. L.C. Morland and P.G. Saffman, J. Fluid Mech. 252, 383 (1993).
12. G.R. Valenzuela, J. Fluid Mech. 76, 229 (1976).
13. E.D. Cokelet, Phil. Trans Roy.Soc. A 286, 183 (1977).
14. B. Chen and P.G. Saffman, Stud. Appl. Math. 62,1 (1980)
15. J.A. Zufiria, J. Fluid Mech. 181, 17 (1987)
16. J. A. Simmen and P. G. Saffman, Stud. App. Math. 73, 35 (1985)
17. F. A. Milinazzo and P.G. Saffman, J. Fluid Mech. 216, 93 (1990)
18. M.L. Banner and O.M. Phillips, J. Fluid Mech.65, 647 (1974)
19. A.F. Teles da Silva and D.H. Peregrine, J. Fluid Mech.195, 281 (1988)
20. A. Baumstein, Symmetry breaking bifurcations in the presence of shear. (In preparation)
21. O.M. Phillips, J. Fluid Mech. 9, 193 (1960).
22. T.B. Benjamin and J.E. Feir, J. Fluid Mech. 27, 417 (1970).
23. M.J. Lighthill, J. Inst. Math. Appl. 1, 269 (1965).
24. V.E. Zakharov, Sov. Phys. J.E.T.P., 51, 1107 (1966).
25. V.E. Zakharov, J. Appl. Mech. Tech. Phys. 2, 190 (1968).
26. M.S. Longuet-Higgins, Proc. Roy. Soc. A360, 471, and 489 (1978).
27. P.G. Saffman, J. Fluid Mech. 159, 169 (1985).
28. R.S. MacKay and P.G. Saffman, Proc. Roy. Soc. A406, 115 (1986).
29. J.W. McLean, Y.C. Ma, D.U. Martin, P.G. Saffman and H.C. Yuen, 1981 Phys. Rev. Lett. 46, 817 (1981).
30. J.W. McLean, J. Fluid Mech. 114, 315 (1982).
31. J.C. Li, W.H. Hui and M.A. Donelan, Nonlinear water waves (Eds K. Horikawa and H. Maruo) Springer-Verlag, 1988.
32. D.J. Benney and K. Chow, Stud. App. Math. 74, 227 (1986).
33. M. Okamura and M. Oikawa, J. Phys. Soc. Japan, 58, 2386 (1989).
34. J.W. McLean, J. Fluid Mech. 114, 331 (1982).
35. J.W. Miles, J. Fluid Mech. 3, 185 (1957).

36. R.E. Esch, J. Fluid Mech. 12, 192 (1962).
37. M.E. Stern and Y.A. Adam, Mem. Soc. Roy. Sci. Liege. Ser 6, 6, 179 (1973).
38. L.C. Morland, P.G. Saffman and H.C. Yuen, Proc. Roy. Soc. A433, 441 (1990).
39. E.A. Caponi, H.C. Yuen, F.A. Milinazzo and P.G. Saffman, J. Fluid Mech. 222, 207 (1991)
40. O.M. Phillips, J. Fluid Mech. 2, 417 (1957).
41. S. Ya. Gertsenshtein, N.B. Romashova and V.M. Chernyavskii, Fluid Dynamics 23, 457, (1988)
42. D. Hill, Inviscid instability of continuous shear profiles at an air-water interface (in preparation).
43. M. Z. Caponi, P. G. Saffman and H. Yuen, Effect of long waves on the stability of wind generated waves, "The Air-Sea Interface", M. A. Donelan, W. H. Hui and W. J. Plant, Eds., The University Press, Toronto, Dec. 1995.
44. H. C. Yuen, Enrico Fermi, Internat. School of Physics, Nonlinear topics in Ocean Physics. July-Aug. Varenna, Italy, 1988; A. Osborn,Ed. North Holland (1991)
45. M. Z. Caponi, Effect of long waves and shear on the generation of waves by wind, ONR Ocean Waves Workshop, Tucson, Arizona, March 1994.
46. Yu. L. Troitskaya, J. Fluid Mech. 273, 169 (1994)
47. M. Z. Caponi and P. G. Saffman, Nonlinear interaction between long waves and short wind generated waves. (In preparation)

RADM Gaffney Is New Chief of Naval Research

Rear Admiral Paul G. Gaffney, II, became the 19th Chief of Naval Research on July 12, 1996, during a change of command at the Washington Navy Yard. He relieved Rear Admiral Marc Pelaez.

In addition to his new position, RADM Gaffney will continue as Commander of the Naval Meteorology and Oceanography Command for the next year. He has held this position since August 1994. He is dividing his time between Office of Naval Research (ONR) Headquarters in Arlington, Virginia, and the Naval Meteorology and Oceanography Command Headquarters in Stennis Space Center, Mississippi.

As the Department of the Navy's senior science and technology executive, RADM Gaffney is responsible for more than a $1 billion science program ranging from basic research, conducted at universities to development of manufacturing technologies. In addition to headquarters, RADM Gaffney's ONR command includes offices in London and Tokyo which provide liaison to the international scientific establishment. Also under his command is the Navy's corporate laboratory, the Naval Research Laboratory (NRL), in Washington, D.C., with branches in Stennis Space Center, Mississippi, and Monterey, California. NRL is a leader in the development of science and technology relevant to all aspects of naval warfare, including control of the seas, littoral areas, naval airspace, the middle atmosphere, and outer space.

Celebrating 50 years of service to the Department of the Navy and the nation, ONR in 1996 meets the unique requirements of the Navy and Marine Corps by supporting research at Navy laboratories and funding research through grants and contracts with universities, industry, and non-profit organizations. ONR provides technical advice to the Chief of Naval Operations and the Secretary of the Navy, works with industry to improve technology and manufacturing processes to reduce fleet costs, and encourages academic interest in naval-relevant science from the high school through post-doctoral levels.

RADM Gaffney is no stranger to ONR. He was the Acting Director of the Arctic and Earth Sciences Division at ONR from November 1980 to August 1981. From May 1989 to February 1991, he served as the Assistant Chief of Naval Research and then as Commanding Officer of NRL. His other assignments have included: tours as Military Assistant to the Assistant Secretary of Defense for International Security Affairs, Commanding Officer of Oceanographic Unit Four survey in Indonesia and Commanding Officer, Naval Oceanography Command Facility Jacksonville, Director of the Oceanography Resources Division on the staff of the Oceanographer of the Navy, and Executive Assistant to the Oceanographer of the Navy.

RADM Gaffney is a 1968 graduate of the U.S. Naval Academy. He received a masters degree in ocean engineering from Catholic University of America, Washington, D.C., and a master's degree in business administration from Jacksonville University, Florida. He graduated with highest distinction from the Naval War College in Newport, Rhode Island in 1979. His awards include the Defense Superior Service Medal, Legion of Merit (three awards), Bronze Star with Combat "V," Meritorious Service Medal and the J. William Middendorf Prize for Strategic Research at the Naval War College.